

**STRUCTURE AND NANOTRIBOLOGY OF
THERMALLY DEPOSITED GOLD
NANOPARTICLES ON GRAPHITE**

A THESIS SUBMITTED TO
THE GRADUATE SCHOOL OF ENGINEERING AND SCIENCE
OF BILKENT UNIVERSITY
IN PARTIAL FULFILLMENT OF THE REQUIREMENTS FOR
THE DEGREE OF MASTER OF SCIENCE
IN
MATERIALS SCIENCE AND NANOTECHNOLOGY

By

Ebru Cihan

July, 2015

STRUCTURE AND NANOTRIBOLOGY OF THERMALLY DEPOSITED
GOLD NANOPARTICLES ON GRAPHITE

By Ebru Cihan

July, 2015

We certify that we have read this thesis and that in our opinion it is fully adequate,
in scope and in quality, as a thesis for the degree of Master of Science.

Assist. Prof. Dr. Mehmet Zeyyad Baykara (Advisor)

Assist. Prof. Dr. Engin Durgun

Assist. Prof. Dr. Cem Çelebi

Approved for the Graduate School of Engineering and Science:

Prof. Dr. Levent Onural
Director of Graduate School

ABSTRACT

**STRUCTURE AND NANOTRIBOLOGY OF
THERMALLY DEPOSITED GOLD
NANOPARTICLES ON GRAPHITE**

Ebru Cihan

M.S. in Materials Science and Nanotechnology

Advisor: Assist. Prof. Dr. Mehmet Zeyyad Baykara

July, 2015

Forming a complete understanding of the physical mechanisms that govern friction on the nanometer and atomic scales is an ongoing endeavor for scientists from various disciplines. While atomic force microscopy (AFM) has proven to be invaluable for the detailed study of nano-scale frictional properties associated with various surfaces, issues related to the precise characterization of the contact formed by the probe tip and the sample surface remain largely unsolved.

In recent years, an alternative approach to nanotribology experiments has involved the lateral manipulation of well-characterized nanoparticles on sample surfaces via AFM and the measurement of associated frictional forces. In line with this idea, ambient-condition structural/nanotribological characterization and nano-manipulation experiments involving gold nanoparticles (AuNP) thermally deposited on highly oriented pyrolytic graphite (HOPG) are presented in this thesis. The effect of deposition amount on thin film morphology is discussed and post-

deposition annealing procedure in terms of different annealing temperatures and times are tackled in order to characterize AuNP formation on HOPG. The morphology and distribution of AuNPs on HOPG are studied via scanning electron microscopy (SEM) while the confirmation of AuNP crystallinity via transmission electron microscopy (TEM) is also described. Topographical characterization of the resulting AuNP/HOPG material system performed via contact-mode AFM is demonstrated. Lateral force measurements are also presented, in terms of the dependence of friction force on normal load as well as the dependence of friction force increase at AuNP edges on normal load and particle height. Subsequent to comprehensive structural and frictional characterization, the results of nano-manipulation experiments performed on AuNPs on the HOPG substrate are reported and it is observed that AuNPs experience remarkably low frictional forces during sliding. A detailed study of friction with respect to contact area firmly confirms the occurrence of *structurally lubric* sliding under ambient conditions for this material system. This result constitutes the first observation of structurally lubric sliding under ambient conditions between different materials in the scientific literature.

Keywords: Atomic force microscopy, Friction force microscopy, Friction, Nanotribology, Nanoparticle, Superlubricity, Structural lubricity

ÖZET

ISIL BUHARLAŞTIRMA İLE ELDE EDİLMİŞ ALTIN NANO PARÇACIKLARIN YAPISAL VE NANOTRİBOLOJİK KARAKTERİZASYONU

Ebru Cihan

Malzeme Bilimi ve Nanoteknoloji Bölümü, Yüksek Lisans

Tez Danışmanı: Yrd. Doç. Dr. Mehmet Zeyyad Baykara

Temmuz, 2015

Nanometre ve atomik ölçeklerde sürtünmeyi kontrol eden fiziksel mekanizmaların daha iyi anlaşılmasını sağlamak, çeşitli disiplinlerden gelen yüzey bilimcileri için süregelen bir çabadır. Atomik kuvvet mikroskopunun (AKM) farklı yüzeyler ile ilişkili nano-ölçekli sürtünme özelliklerinin karakterizasyonunda kullanımı oldukça değerli olduğu halde, prob ucu ile numune yüzeyi arasında oluşan temasın detaylı karakterizasyonu ile ilgili sorunlar büyük ölçüde çözülememiştir.

Son yıllarda nanotriboloji deneyleri için AKM tekniği kullanılarak, numune yüzeylerinde konuşlanmış ve iyi karakterize edilmiş nano parçacıkların yanıl manipülasyonu sırasında sürtünme kuvvetlerinin ölçümünü kapsayan alternatif bir yaklaşım geliştirilmiştir. Bu fikir doğrultusunda, bu tezde, ortam koşulları altında, yüksek yönelimli pirolitik grafit (HOPG) üzerinde ısıl olarak biriktirilmiş altın nano parçacıkların (AuNP) yapısal ve tribolojik karakterizasyonu ile nano-

manipülasyon deneylerini içeren çalışmalar sunulmuştur. Grafit üzerindeki altın nano parçacık oluşumunu karakterize edebilmek için depozisyon miktarının ince film morfolojisi üzerindeki etkisi incelenmiş; aynı zamanda farklı tavlama sıcaklığı ve sürelerinin ısı biriktirme sonrası gerçekleştiren tavlama prosedürünün sonuçlarına etkisi incelenmiştir. Altın nano parçacıkların grafit üzerindeki dağılımı ve morfolojisi taramalı elektron mikroskopisi (SEM) yardımı ile incelenmiş, parçacıkların kristalin yapıda oldukları geçirimli elektron mikroskopisi (TEM) yardımı ile de doğrulanmış ve topografik karakterizasyonları da temaslı AKM tekniği ile gerçekleştirilmiştir. AuNP/Grafit malzeme sisteminde sürtünme kuvvetlerinin uygulanan normal kuvvete bağlılığı ölçülmüş, altın nano parçacık kenarlarında gerçekleşen ani sürtünme kuvveti artışlarının hem uygulanan normal kuvvete hem de nano parçacık yüksekliğine bağlılığı incelenmiştir. Altın/Grafit malzeme sisteminin bu kapsamlı yapısal ve nanotribolojik karakterizasyonunun ardından, grafit üzerinde konuşlanmış altın nano parçacıklar üzerinde gerçekleştirilen nano-manipülasyon deneylerinin sonuçları rapor edilmiş ve altın nano parçacıkların grafit üzerinde kayarken çok düşük sürtünme kuvvetlerine maruz kaldıkları gözlemlenmiştir. Bahsi geçen sürtünme kuvvetleri, temas alanına bağlı olarak detaylı bir şekilde incelendiğinde, bu malzeme sisteminin ortam koşullarında *yapısal kayganlık* gösterdiği kanıtlanmıştır. Bu sonuç, bilimsel literatürde ortam koşullarında farklı malzemeler arasında *yapısal kayganlığın* ilk olarak gözlemlenmesi anlamına gelmektedir.

Anahtar Kelimeler: Atomik kuvvet mikroskopisi, Sürtünme kuvvet mikroskopisi, Sürtünme, Nanotriboloji, Nano parçacık, Süperkayganlık, Yapısal kayganlık

Acknowledgement

First and uppermost I would like to thank my academic advisor, Prof. Mehmet Zeyyad Baykara, for his valuable support and guidance as well as his sincere communication throughout my dissertation. He has been a great leader for me and provided me with a broad view of our scientific field and community. I believe that his open-minded and enthusiastic approach to research has had worthy contributions to my perspective on science.

I have enjoyed working in the laboratory and exchanging opinions with the many creative and talented people of the Scanning Probe Microscopy (SPM) research group. So, I would also like to thank our group members Arda Balkancı, Tuna Demirbaş, Tarek Abdelwahab, Alper Özoğul, Berkin Uluutku, Zeynep M. Süar and Verda Saygın for their kind friendship.

And of course, I would like to thank all other faculty members, students and engineers of UNAM-National Nanotechnology Research Center for their contributions.

I would like to express my gratitude to the National Nanotechnology Research Center (UNAM) for the M.S. Scholarship I have benefited throughout my M.S. and also gratefully acknowledge financial support for my research activities received by Prof. Baykara from the Marie Curie Actions of the European Commission's FP7 Program in the form of a Career Integration Grant and the Outstanding Young Scientist program of the Turkish Academy of Sciences (TÜBA-GEBİP).

Last but not least, I would like to thank my family for their endless love and support throughout this rocky road. For sure, I have the best mother in the world who never gives up being at my elbow. I am so grateful for all she taught me and being such a person. And of course, I could not think of a life without my lovely

sister. She has always been another primary believer along my life left behind and will keep on this as far as I understand from our cheerful telephone conversations.

To my dear family

Contents

Acknowledgement.....	VII
List of Figures	XII
List of Tables.....	XVI
1. Introduction	1
1.1 Overview	1
1.1.1 Friction: History and Physical Principles	3
1.1.2 Nanotribology: The Science of Friction, Lubrication, and Wear on the Nano-scale	5
1.2 Outline	8
2. Principles of Atomic Force Microscopy.....	10
2.1 Background.....	10
2.2 Basic Operating Principle of AFM: Contact Mode	13
2.3 Measuring Lateral Forces via Friction Force Microscopy	19
3. Selection of Materials: Gold on Graphite	21
3.1 Highly Oriented Pyrolytic Graphite: Structure and Physical Properties ..	21
3.2 Gold: Structure and Physical Properties	24
3.3 The Au/HOPG Material System.....	25
4. Preparation and Structural Characterization of Gold Nanoparticles.	29
4.1 Background.....	29
4.2. Thermal Evaporation	31
4.2.1 Basic Principle and Experimental Parameters.....	31
4.2.2 Effect of Deposition Amount on Thin Film Morphology	33
4.3 Formation of AuNPs by Post-Deposition Annealing	36
4.4 Structural Characterization of AuNPs	39

4.4.1 Determination of AuNP Size Distribution via Scanning Electron Microscopy	39
4.4.2 Confirmation of AuNP Crystallinity via Transmission Electron Microscopy	40
4.4.3 Topographical Characterization of AuNPs via Contact Mode AFM	43
5. Frictional Characterization of the AuNP/HOPG Material System	47
5.1 Background.....	47
5.2 Force Sensor Calibration	49
5.2.1 Normal Spring Constant Calibration	49
5.2.2 Lateral Force Calibration.....	50
5.3 Lateral Force Measurements on the AuNP/HOPG Material System	51
5.3.1 Dependence of Lateral Force on Normal Load for AuNPs and HOPG	54
5.3.2 Dependence of Increased Lateral Forces at AuNP Edges on Normal Load and Particle Height	58
5.4 Force-Distance Spectroscopy Experiments for the Characterization of Adhesion on AuNPs	60
6. Nano-Manipulation Experiments on the AuNP/HOPG Material System: Contact Area Dependence and Structural Lubricity	62
6.1 Background.....	62
6.2 Manipulation of AuNPs on HOPG.....	64
6.2.1 Basic Principle.....	64
6.2.2 Repeatability.....	68
6.3 Contact Area Dependence of Friction: Structural Lubricity under Ambient Conditions.....	69
7. Summary and Outlook.....	75
Bibliography.....	77

List of Figures

Figure 1.1 An illustration of two seemingly flat surfaces in contact sliding against each other	2
Figure 1.2 Leonardo da Vinci (1452-1519), Guillaume Amontons (1663-1705), Charles-Augustin Coulomb (1736-1806).....	4
Figure 1.3 A basic illustration of an atomic force microscopy in which the single asperity contact between the AFM tip and the sample surface is demonstrated.....	6
Figure 2.1 Nobel Laureates Gerd Binnig and Heinrich Rohrer with the first STM that they built; together with other notable SPM inventors Christoph Gerber and Calvin F. Quate	12
Figure 2.2 Schematic illustrating the general working principle of a typical AFM	15
Figure 2.3 A close-up picture of a Si AFM tip from the side via SEM	16
Figure 2.4 A topography map recorded during contact mode AFM scanning of a HOPG sample decorated with AuNPs.	16
Figure 2.5 Schematic of a typical force-distance curve acquired with a static cantilever	18
Figure 2.6 An illustration of torsional twisting undergone by the cantilever of the AFM during scanning to the left and right on a sample surface	19
Figure 2.7 An example of a friction loop formed by lateral forces recorded during forward and backward scans along the lateral x-axis.....	20

Figure 3.1 (a) A single graphene layer where the hollow sites and carbon atoms in the honeycomb structure are indicated, (b) schematic describing the structure of bulk graphite.....	23
Figure 3.2 A typical topographical map of the HOPG (0001) surface recorded with contact mode AFM, showing large, flat terraces.	23
Figure 3.3 (a) FCC crystal structure of gold, (b) a high-resolution, cross-sectional TEM image of a Au nanoparticle exhibiting (111) planes with inter-atomic distance of 2.36 Å.....	25
Figure 3.4 An illustration of the principle of structural lubricity	26
Figure 3.5 (a) SEM image of the HOPG substrate after thermal deposition of 1 Å Au, resulting in a channeled thin film, (b) SEM image of the HOPG substrate decorated with crystalline AuNPs of various sizes after post-deposition annealing.	27
Figure 3.6 Schematic drawing emphasizing the suitability of the Au/HOPG material system for nano-manipulation experiments based on lattice mismatch and the particularly low surface energy of HOPG.....	28
Figure 4.1 (a) Au film deposited on air-cleaved graphite at room temperature, 9.9 Å, (b) Au film deposited on vacuum-cleaved graphite at room temperature, 9.9 Å, (c) Au film deposited on air-cleaved graphite at 450 °C, 168 Å, (d) Au film deposited on vacuum-cleaved graphite at 450 °C, 168 Å	30
Figure 4.2 Thermal Evaporator, Vaksis PVD Vapor-3S.....	32
Figure 4.3 The SEM instrument used for the experiments presented in this thesis (FEI Quanta 200 FEG)	34

Figure 4.4 SEM images of as-deposited Au thin films on HOPG for total deposition amounts of (a) 20 Å, (b) 10 Å, (c) 5 Å, (d) 1 Å.....	35
Figure 4.5 Surface coverage of Au on HOPG as a function of film thickness	36
Figure 4.6 Quartz tube furnace used for post-deposition annealing.....	37
Figure 4.7 SEM images of the AuNP/HOPG material system after post-deposition annealing in quartz furnace at (a) 500 °C for 30 min., (b,c) 600 °C for 2 h and (d) 650 °C for 2h.....	38
Figure 4.8 AuNP size distribution after post-deposition annealing at 600-650 °C.....	39
Figure 4.9 The TEM instrument used for the experiments presented in this thesis (FEI Technai G2 F30)	41
Figure 4.10 The FIB instrument used for the experiments presented in this thesis (FEI Nova 600i Nanolab).....	42
Figure 4.11 (a) TEM measurements performed on a single, well-faceted AuNP, (b) high resolution image at the edge of the AuNP, (c) associated electron diffraction pattern, (d) cross-sectional, high-resolution TEM image clearly demonstrating crystalline order and the absence of an oxide layer on the AuNPs	43
Figure 4.12 The AFM instrument used for the experiments presented in this thesis (PSIA XE-100E)	44
Figure 4.13 (a) Large scale contact mode AFM topography image of the AuNP/HOPG system, exhibiting immobile AuNPs as well as an unintentional manipulation event, (b) contact mode AFM topography image of two AuNPs stuck between HOPG step edges	45

Figure 4.14 (a) Topographical map of a 75 nm high AuNP trapped between HOPG steps acquired via contact-mode AFM and (b) its 3D representation	46
Figure 5.1 Schematic diagram of TGF11 silicon calibration grating	51
Figure 5.2 Illustration of the AFM tip scanning the AuNP/HOPG material system in contact mode. (a) AFM tip approaches the AuNP, (b) AFM tip is on the AuNP and (c) AFM tip leaves the NP behind and continues scanning on the HOPG substrate.....	52
Figure 5.3 A representative, large-scale lateral force map of the AuNP/HOPG material system.....	53
Figure 5.4 (a) Friction force map recorded on a region of the sample surface containing a hexagonal AuNP stuck between the step edges of HOPG and (b) the friction force profile along the dashed black arrow in (a).....	54
Figure 5.5 Experimental data demonstrating the dependence of friction force (F_f) on normal load (F_n) for AuNPs as well as the HOPG substrate.....	56
Figure 5.6 An idealized single asperity contact involving a spherical tip apex and a flat surface	57
Figure 5.7 Experimental data demonstrating the dependence of increased friction forces at AuNP edges ($F_{f,edge}$) on AuNP height (h), acquired at a fixed normal load of 13.8 nN	59
Figure 5.8 Experimental data demonstrating the dependence of increased friction forces at AuNP edges ($F_{f,edge}$) on normal load (F_n) for a representative AuNP with 128 nm height.....	60
Figure 5.9 A force-distance spectroscopy curve acquired on an individual AuNP.	61

Figure 6.1 Illustration of the AFM tip approaching and manipulating a AuNP on the HOPG substrate. (a) AFM tip scans the HOPG surface and approaches the AuNP, (b) AFM tip reaches the AuNP while the particle is still stationary, (c) manipulation event is achieved and AFM tip pushes the AuNP laterally on the HOPG substrate: (1) before manipulation, (2) after manipulation..... 65

Figure 6.2 (a) Illustration of the lateral manipulation process of a AuNP on the HOPG via contact-mode AFM. Topography and lateral force data measured (b) before and (c) during the manipulation (along the orange arrow) 67

Figure 6.3 Illustration of the repeatable manipulation process of an individual AuNP between two HOPG steps. (a) Lateral force map recorded during the multiple manipulation of the AuNP between two HOPG steps. (b) Average lateral forces extracted for 12 separate profiles taken from the area inside the white dashed rectangle displayed in (a) 68

Figure 6.4 Friction forces for 37 AuNPs during sliding on the HOPG substrate as a function of particle contact area 71

Figure 6.5 Normalized friction data from lateral manipulation experiments plotted as a function of N , the number of atoms on the sliding surface of AuNPs 72

Figure 6.6 Normalized friction data from lateral manipulation experiments plotted as a function of N , the number of atoms on the sliding surface of AuNPs 73

List of Tables

Table 4.1 Physical vapor deposition parameters for the Au deposition 32

Table 5.1 Physical properties of the Si cantilever used in the FFM experiments .. 50

Chapter 1

Introduction

1.1 Overview

Friction is a phenomenon that we face frequently in our daily lives, with great importance for seemingly simple tasks such as walking and playing an instrument. Furthermore, friction has fundamental importance for various technological fields in a great range of dimensions, all the way from car engines and fundamental manufacturing processes such as forging and extrusion, to advanced devices including micro- and nanoelectromechanical systems (MEMS/NEMS). Besides, friction plays a great role for the proper functioning of a great variety of biological systems and processes, including mechanical interactions between cells and the proper functioning of the musculoskeletal system in humans and other animals.

Friction can be defined as a “physical resistance” against the relative movement of two solid surfaces in contact against each other. The “physical resistance” in question is often described as a *friction force* (F_f) that can be macroscopically measured via simple experimental setups. The fundamental physical process behind friction occurring during sliding contact involves the dissipation of energy as the kinetic energy associated with the motion is transformed to thermal energy

via friction. As a practical manifestation of this principle, this characteristic of friction has been utilized since ancient times to obtain fire by rubbing two pieces of wood against each other.

Despite its fundamental and practical importance, the governing principles behind friction have not been clearly understood yet [1]. A particular problem associated with the interpretation of macroscopic friction experiments (performed commonly by sliding a block of a given shape over a seemingly flat surface) involves the fact that all surfaces (even those that seem to be perfectly flat to the naked eye) ultimately feature a degree of roughness, that results in a *multi-asperity* nature, as seen in Figure 1.1. As such, the *real* contact area (A) is much smaller than the *apparent* one (A_{apparent}) as it is formed only due to the contact between a small number of asperities on the contacting surfaces. As the determination of A is not straightforward in macroscopic friction experiments, the use of scanning probe microscopy (SPM) methods has been rapidly increasing in the area of friction investigation in the last two decades, since the *probe* used in the experiments represents a *single-asperity* dimensions of which can be measured with a given degree of certainty.

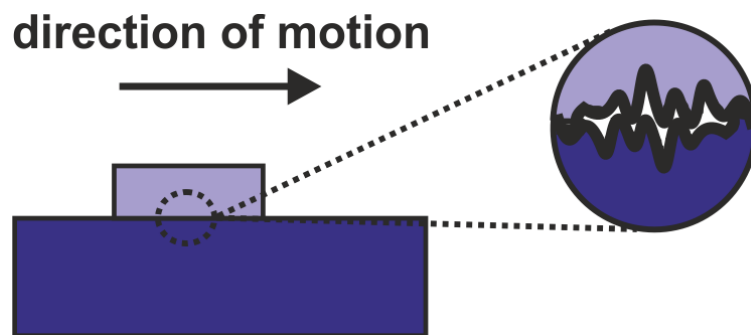


Figure 1.1 An illustration of two seemingly flat surfaces in contact sliding against each other. The zoomed-in view of the interface emphasizes the multi-asperity nature of the two surfaces and the resulting, real contact area A .

In this M.S. thesis, the aim is to contribute to the further understanding of physical laws and processes that govern the phenomenon of friction, by presenting the results of nanometer-scale structural and frictional characterization studies performed on gold nanoparticles (AuNPs) on highly oriented pyrolytic graphite (HOPG), performed via atomic force microscopy (AFM). The following parts of this introductory chapter further emphasize the history and physical principles of friction and provide an outline for the rest of the thesis.

1.1.1 Friction: History and Physical Principles

As indicated earlier, the universal phenomenon of friction is frequently encountered in everyday activities as well as industrial processes. One should also emphasize that friction is the main source of energy dissipation during many different industrial processes, causing it to have a substantial economic impact on world economy [1].

As one can always encounter friction in nature, the study of this particular phenomenon has drawn attention for hundreds of years. Leonardo da Vinci (1452-1519) who can be considered the father of modern *tribology* (the science of friction, wear and lubrication) has studied friction, wear and lubrication, particularly in bearings and discovered certain classical rules of sliding friction that are still taught in high schools today. However, Da Vinci has not published his results. About 150 years later, “Amontons’ Laws of Friction” have been introduced [2]. Guillaume Amontons (1663-1705) explained the nature of macroscopically observed friction as independent from apparent contact area, but linearly dependent on the *normal load* (F_n) that is pressing the surfaces together. Accordingly, Amontons’ first law describes that the friction force is directly proportional to the applied load and the second law of Amontons emphasizes that the friction force is independent of the contact area. Those observations have been further developed by Belidor (1698-1761), modeling friction associated with a rough surface with

spherical asperities. The first distinction between kinetic and static friction has been made by Leonard Euler (1707-1783). Those discoveries have been further developed by Charles-Augustin Coulomb (1736-1806). Coulomb has studied in detail the effects of four fundamental parameters on friction which are the structural nature of the surfaces in contact, the size of the contact area, the normal load acting between the surfaces and the time that the surfaces have spent in contact. Moreover, he has taken into account the effect of sliding velocity as well as environmental conditions such as temperature and humidity on the friction behavior. Ultimately, he has introduced “Coulomb’s Law of Friction” which indicates that kinetic friction is independent of the sliding velocity [3].

The fundamental and classical laws of macroscopic friction have been summarized by Isaac Newton via the introduction of a friction coefficient μ that depends only on the materials out of which the surfaces in contact are made and acts as the proportionality constant between the friction force, F_f , and the normal load, F_n [4]:

$$F_f = \mu F_n \quad (1.1)$$

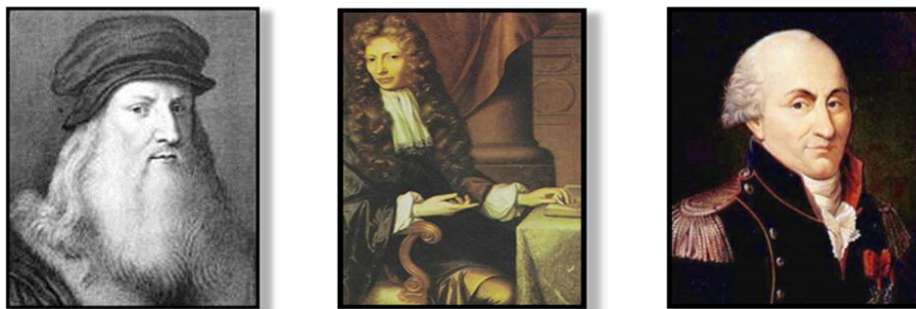


Figure 1.2 Leonardo da Vinci (1452-1519), Guillaume Amontons (1663-1705), Charles-Augustin Coulomb (1736-1806).

Although the classical macroscopic law of friction involving a linearly proportional relationship between the friction force and the normal load have been well constituted (Equation 1.1), the friction coefficient which is be macroscopically observed can not to be derived from first principles [1]. Besides, as indicated earlier, the multi-asperity nature of the interface between two macroscopic surfaces in contact makes it problematic to determine the actual contact area between the two surfaces [5]. To tackle the problem of friction under better defined conditions, the field of *nanotribology* has been introduced, which is introduced in the next section.

1.1.2 Nanotribology: The Science of Friction, Lubrication, and Wear on the Nano-scale

As introduced earlier, *tribology* is an interdisciplinary scientific field of inquiry that deals with friction, lubrication, and wear. Consequently, if tribological studies are performed on the nanometer scale (1-100 nm) with the aim of elucidating the fundamental working mechanisms of friction, the term *nanotribology* is used to designate the associated scientific efforts.

Despite the fact that tribology experiments have been first performed hundreds of years ago, the classical laws of macroscale friction developed in this fashion could not be satisfactorily explained from first principles. One of the associated major problems has been the multi-asperity nature of macroscopic contacts that are virtually composed of lots of individual, nano-/micro-scale single-asperities. As such, in order to understand the fundamental mechanism located at the heart of friction, observations of single-asperity contacts are essential. That is where the method of atomic force microscopy starts to play an important role.

After the invention of the atomic force microscopy and its use in the measurement of friction in a manifestation of the method called friction force microscopy (FFM, first introduced in 1987 by Mate et al. [6]), the research field of nanotribology has

been established [7, 8]. From that point on nanotribology studies have been performed via AFM/FFM to investigate the fundamentals of friction on the nanoscale. The main advantage offered by AFM for the measurement of friction is the fact that it provides a nanometer-scale, single-asperity (the *tip* of the AFM), with which to measure lateral forces (and thus, friction) on sample surfaces with great spatial (nm) and force (sub-nN) resolution (Figure 1.3).

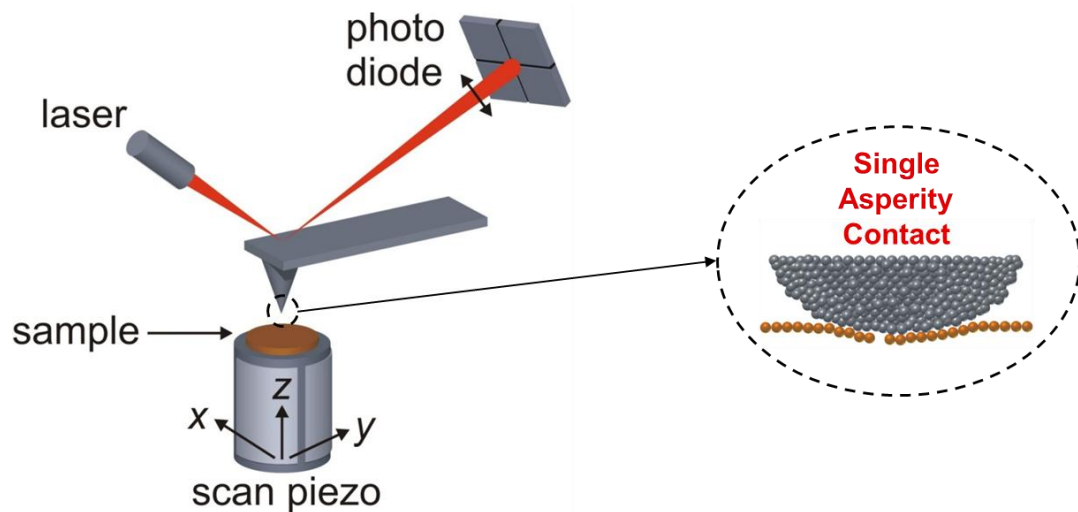


Figure 1.3 A basic illustration of an atomic force microscopy in which the single asperity contact between the AFM tip and the sample surface is demonstrated [9].

Despite the fact that FFM has been utilized with great success since its invention to discover fundamental tribological phenomena such as *stick-slip* [10] and *superlubric sliding* [11], there are certain limitations to its usefulness:

1. The chemical composition and the structure of the probe tip apex cannot be determined with atomic precision.
2. AFM tip materials are very limited (Si, SiO₂, Si₃N₄, etc.) restricting the study of frictional behavior of different types of materials.

Accordingly, as an alternative to *typical* FFM experiments, measuring the frictional behavior of a material system consisting of nanoparticles localized on a flat substrate via the lateral manipulation of the nanoparticles using AFM appears as a good strategy [12]. While conventional FFM only measures friction at the interface between the AFM tip and the surface, nanoparticle manipulation via AFM and the measurement of friction forces during manipulation allow the examination of friction at larger, structurally well-defined interfaces between the nanoparticles and the substrate surface.

Contrary to the limited choice of cantilever materials, there are no hard restrictions on the selection of nanoparticle materials measured via the method described above. While AFM tips can be coated by metals such as Au to achieve varying contact areas in typical FFM measurement, coated tips tend to be more prone to degradation by wear or contamination and structurally complicated to characterize, causing inconsistencies in measured friction values [12].

Additionally in conventional FFM studies, the real contact area between the AFM tip and the surface cannot be precisely determined due to the lack of a suitable method to measure it and this prevents a thorough and complete investigation of the dependence of friction on real contact area in nanotribology experiments. Additionally, recalling that the macroscopically measured friction forces appear to be independent of apparent contact area, this potential dependence of friction on real contact area becomes even more remarkable and worthy of investigation. The method based on the manipulation of nanoparticles on a substrate surface is particularly suitable here. It allows the accurate measurement of the actual contact area between the nanoparticle and the substrate, especially if the nanoparticles have been deposited on the substrate by a method such as thermal evaporation leading to the occurrence of commensurate interfaces [12]. The nanoparticles can be produced to be either crystalline or amorphous dependent on the material and deposition parameters [13]. Relatively low particle-substrate interaction should be achieved to

readily manipulate nanoparticles by inhibiting adsorbing them by the substrate surface. Highly oriented pyrolytic graphite (HOPG) or molybdenum disulfide (MoS_2) are mostly used as substrates thanks to their atomically flat, large terraces in which nanoparticles are allowed to move along in addition to their low surface free energies. When a convenient material system is obtained, the lateral manipulation of nanoparticles on the flat substrate is performed via pushing by the AFM tip and the interfacial friction between the nanoparticle and the substrate is measured [12].

In this M.S. thesis, nano-manipulation experiments have been performed on crystalline AuNPs thermally deposited on HOPG and the associated frictional behavior has been quantified under ambient conditions. As explained in detail in Chapter 6, the results remarkably point towards *superlubric sliding* of AuNPs on graphite.

1.2 Outline

After the introduction to the subjects of friction and nanotribology initiated in this chapter, the thesis will proceed with Chapter 2 (Principles of Atomic Force Microscopy) in which the basic operating principle of contact mode AFM is investigated. Measurement of lateral forces via AFM during raster-scanning of the surface will also be handled.

Chapter 3 (Selection of Materials: Gold on Graphite) will describe the reasoning behind the selection of the AuNP/HOPG material system for the nanotribological studies presented in this thesis, based on the structure and physical properties of both gold and graphite.

Chapter 4 contains information regarding the preparation and structural characterization of AuNPs. This chapter will start with a review of background literature and then will continue with results regarding thermal deposition of Au

onto the HOPG substrate. The effect of deposition amount on thin film morphology will be discussed and post-deposition annealing procedure in terms of different annealing temperatures and times will be tackled in order to characterize AuNP formation on HOPG. The morphology and distribution of AuNPs on HOPG are studied via scanning electron microscopy (SEM) while the confirmation of AuNP crystallinity via transmission electron microscopy (TEM) will also be described. Finally, topographical characterization of AuNPs performed via contact-mode AFM will be demonstrated.

Chapter 5 will report the frictional characterization of the Au/HOPG material system; hence, the force sensor calibration of both the normal spring constant and the lateral force signal will be explained first. Subsequently, lateral force measurements on the Au/HOPG material system will be presented, in terms of the dependence of friction force on normal load as well as the dependence of friction force increase at AuNP edges on normal load and particle height. Before finalizing this chapter, force-distance spectroscopy experiments will be presented in order to characterize adhesion forces typically encountered on AuNPs.

In Chapter 6 (Nano-Manipulation Experiments on the Au/HOPG Material System: Contact Area Dependence and Structural Lubricity), the results of manipulation experiments of AuNPs on the HOPG substrate will be presented after a review of background studies. Repeatability of measured friction forces during manipulation events for a single AuNP will also be discussed to emphasize the consistency of experimental data. Furthermore, the dependence of friction forces on real contact area for 37 AuNPs will be studied where the fact that AuNPs experience ultra-low friction (consistent with the theory of structural lubricity) even under ambient conditions is encountered.

Ultimately, Chapter 7 will conclude the thesis by providing a summary and an outlook including the future research aspects.

Chapter 2

Principles of Atomic Force Microscopy

2.1 Background

The atomic force microscopy (AFM) was developed in 1986 by scientists at Stanford University and IBM (Gerd Binnig, Christoph Gerber and Calvin F. Quate) [14], subsequent to the invention of the scanning tunneling microscopy (STM) by Gerd Binnig and Heinrich Rohrer in the early 1980s [15].

Basically, STM measures the quantum mechanical tunneling current acting between a probe tip and a (semi-)conductive sample surface under the application of a bias voltage and at typical tip-sample separations of < 1 nm. STM uses the magnitude of the tunneling current as a feedback parameter during raster-scanning, resulting in the acquisition of sub-nm resolution “topography images”, corresponding to contours of constant tunneling current, and consequently, local density of states (LDOS) of electrons. Despite the fact that its operation is quite straightforward and the resulting real-space resolution very good, the main disadvantage of this technique is that insulating materials cannot be studied via its application, due to the lack of a tunneling current. Additionally, measurement of interaction forces cannot be accomplished via STM. On the other hand, AFM

overcomes both limitation via its basic operational principle based on interaction force sensing, which is independent of sample conductivity.

In addition to the capability of high-resolution imaging thanks to the detection of interaction forces during the scanning of the sample surface experienced by a nanometer-scale probe tip typically located at the end of a micro-machined cantilever, the AFM method has led to various manifestations aimed at investigating the mechanical, electrical and magnetic properties of material surfaces at (sub-)nm length scales (see, *e.g.*, the magnetic force microscopy (MFM) or the electrostatic force microscopy (EFM)) [16]. Among the various manifestations of the AFM method, the most relevant for this thesis is the friction force microscopy (FFM) that was invented by Mate and co-workers in 1987 [6], allowing the measurement of *both* normal and lateral forces acting on the probe tip during sample scanning under single-asperity contact, thus paving the way for nanotribology studies. In this chapter, the basic operational principle associated with AFM and its FFM mode will be reviewed.

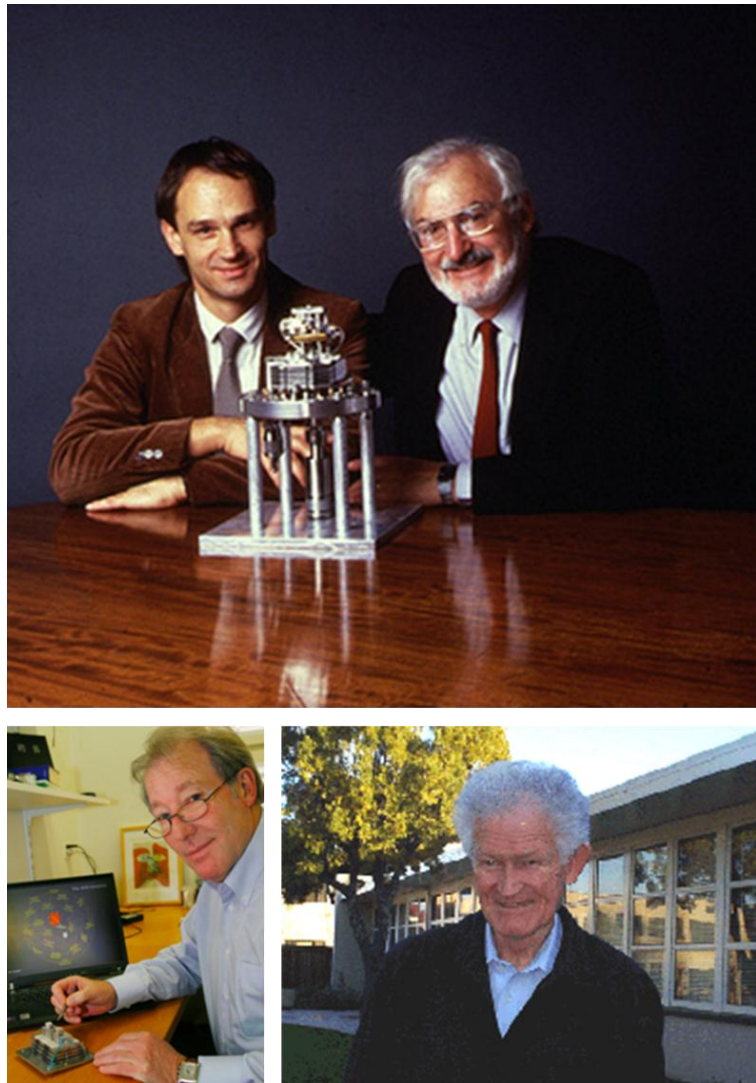


Figure 2.1 Nobel Laureates Gerd Binnig (top left) and Heinrich Rohrer (top right) with the first STM that they built; together with other notable SPM inventors Christoph Gerber (bottom left) and Calvin F. Quate (bottom right). Pictures taken from [17-19].

2.2 Basic Operating Principle of AFM: Contact Mode

In its most fundamental mode of operation (called the *contact mode*), the AFM functions by raster-scanning a sharp, nanometer-scale tip situated at the end of a flexible, micro-machined cantilever over a sample surface of interest and with pm precision under contact by utilizing piezoelectric scan elements (such as a *piezotube*) [16]. During scanning, the normal (vertical) interaction force acting between the tip and the sample is detected by recording the position of a laser beam deflected off the backside of the cantilever on a photodiode, corresponding to the vertical deflection of the cantilever due to the interaction. The general schematic associated with a typical AFM setup is given in Figure 2.2, whereas Figure 2.3 provides an SEM image of a typical AFM tip. By keeping the normal interaction force constant during scanning, (sub-)nm resolution topographical maps of sample surfaces are routinely obtained, as seen in Figure 2.4.

During scanning, the piezoelectric tube is displaced in the vertical (normal) z -direction based on a feedback loop aiming to keep the normal force signal (as determined by the photodiode reading) and a defined force set point (usually on the order of a few nN) equal. Within this picture, please note that the axis parallel to the longitudinal dimension of the cantilever refers to the y -axis while the axis perpendicular to the cantilever length is referred to as the x -axis.

As one can see from Figure 2.2, during scanning, the AFM tip and the sample can be moved with respect to each other, in three (x , y , z) directions and their displacements are converted from applied voltages into actual lengths by the piezoelectric constants associated with the scan tube. The normal force between the AFM tip and the sample surface can be detected by the amount of cantilever deflection using the photo diode approach, as explained earlier. The photo diode

(also referred to as the *photo detector*, PD) consists of 4 quadrants, termed A, B, C, D.

Thanks to the four quadrant structure of the photodiode, it is possible to detect not only the vertical deflections of the cantilever due to normal interaction forces (F_n), but also torsional twisting due to lateral interaction forces (F_l) crucial for FFM become detectable.

In order to measure the normal forces acting between the AFM tip and the sample surface and the resulting vertical cantilever deflection, the difference between the voltage signals coming from the upper quadrants “(A+B)” and the lower quadrants “(C+D)” (U_z) is used:

$$F_n \sim U_z \sim ((A+B) - (C+D)) \quad (2.1)$$

In other respects, the lateral force signal is related to the twisting of the cantilever during scanning and can be measured by the difference between the voltage signals coming from the quadrants on the left “(A+C)” and the quadrants on the right “(B+D)”:

$$F_l \sim U_x \sim ((A+C) - (B+D)) \quad (2.2)$$

On the other hand, one should note that other operational modes of AFM exist where the cantilever is deliberately oscillated near its resonance frequency and tip-sample interactions are measured by tracking changes in oscillation characteristic such as amplitude and frequency. Such AFM modes are commonly grouped under the title *dynamic AFM* which includes the so-called *tapping* and *noncontact* modes [20]. While dynamic AFM modes certainly have advantages in terms of high resolution and reduction in sample and tip damage, the basic advantage of contact mode AFM that is relevant for our experiments is the fact that it *directly* measures F_n and F_l values.

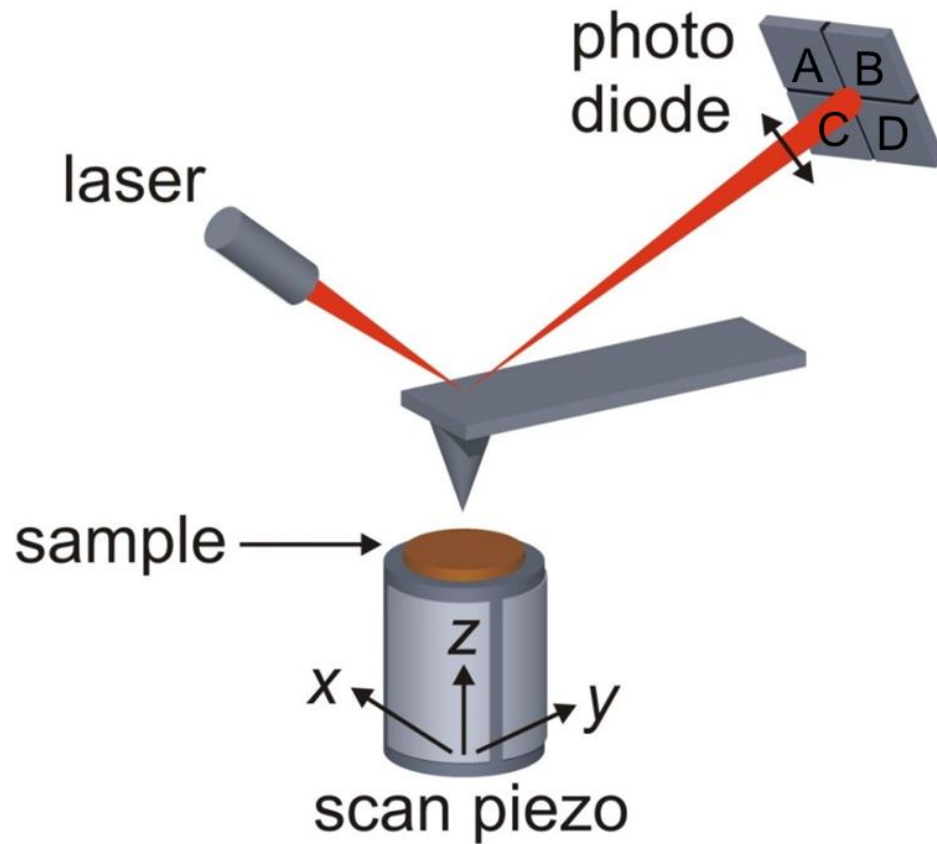


Figure 2.2 Schematic illustrating the general working principle of a typical AFM. The sample is mounted to a piezoelectric tube (the *scan piezo*) and a sharp, nanometer-scale tip attached to a flexible, micro-machined cantilever is used to raster-scan the surface. The deflection of the cantilever in the vertical direction and its torsional twisting due to lateral forces are detected by a four-quadrant PD. Keeping the normal force constant during scanning via a feedback loop results in the acquisition of topographical maps by tracking the z -position of the scan piezo.

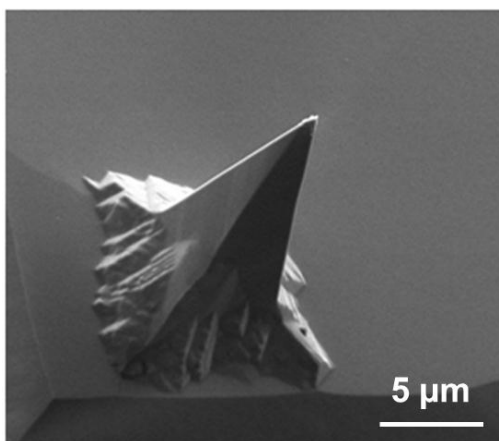


Figure 2.3 A close-up picture of a Si AFM tip from the side via SEM.

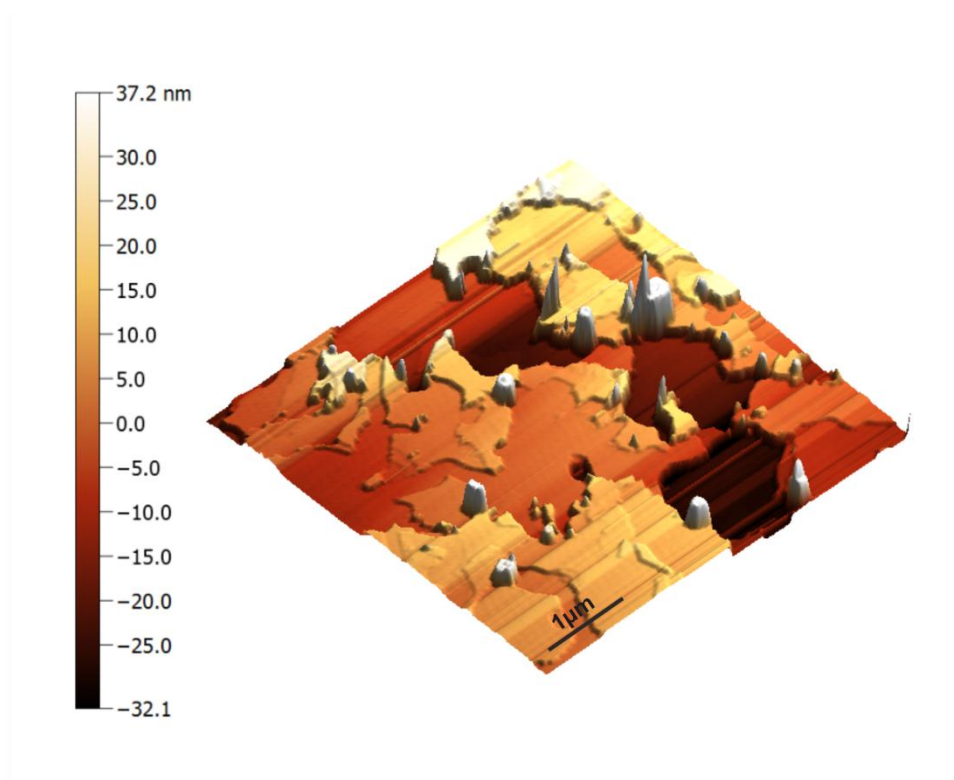


Figure 2.4 A topography map recorded during contact mode AFM scanning of a HOPG sample decorated with AuNPs.

With the AFM, it is not only possible to image sample surfaces with high-resolution, but it also becomes possible to study tip-sample interactions as a function of physical parameters such as tip-sample distance and bias voltage. Such experiments are grouped under the main heading of *force spectroscopy*. It should be noted that a variety of interaction forces including electrostatic, magnetic, mechanical/elastic, van der Waals and short-range chemical interactions may contribute to the detected total force during AFM measurements [21]. Nevertheless, during contact-mode scanning of typical samples surfaces, the mechanical/elastic forces dominate the sample interaction, deflecting the cantilever in the normal z -direction like a leaf spring. Within this context, it should be noted that repulsive forces causing the cantilever to be deflected away from the sample surface are taken as *positive*.

According to Bhushan et al. [21] and as discussed earlier, a linear relationship exists between the measured voltage difference “((A+B) - (C+D))” (U_z) and the normal force (F_n) as shown in Equation 2.3:

$$F_n = (\theta_z U_z) - F_{n,\text{ref}} \quad (2.3)$$

A similar, linear relationship is valid for the measured voltage difference “((A+C) - (B+D))” (U_x) and the lateral force (F_l) as shown in Equation 2.4:

$$F_l = (\theta_x U_x) - F_{l,\text{ref}} \quad (2.4)$$

θ_x is a lateral force calibration factor which can be obtained by a specialized calibration method as explained in Chapter 5. The offset values for both normal and lateral forces, $F_{n,\text{ref}}$ and $F_{l,\text{ref}}$, respectively, are set to zero by proper alignment of the laser spot on the PSPD in order to provide the *unengaged* situation. Please note that the calibration approach to determine the normal spring constant of the cantilever (k_z) is also provided in Chapter 5.

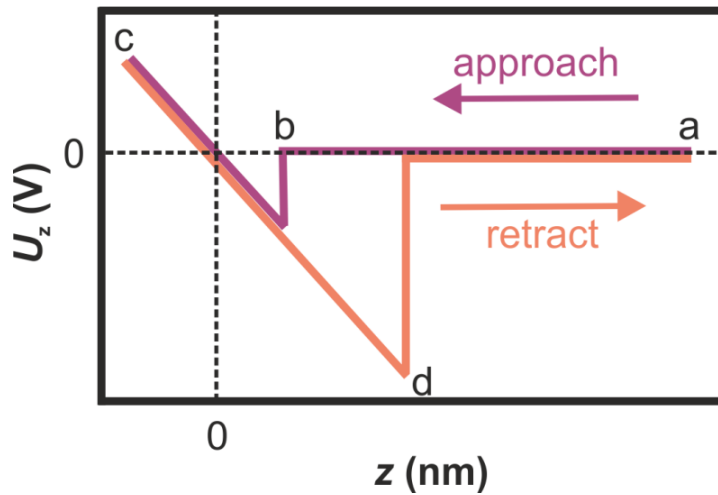


Figure 2.5 Schematic of a typical force-distance curve acquired with a *static* cantilever. The experiment begins at point (a) when the AFM tip is far away from the surface. The tip is then approached to the surface between points (a) and (b). At point (b), the tip *jumps into contact* with the surface. A linear increase of the deflection signal is obtained between points (b) and (c) due to repulsive interaction forces. Subsequently, the tip is retracted from the surface (c) and finally, when the attractive interaction force (the *pull-off* force) surpasses tip-sample adhesion, the tip is released from the surface.

The relationship between the measured voltage signal (U_z) and the normal deflection of the cantilever can be determined from force-distance spectroscopy experiments (Figure 2.5). Firstly, a large amount of distance between the AFM tip and the sample surface is arranged such that the interaction and consequently, U_z is zero (point a in Figure 2.5). Then the tip is approached to the surface and the distance is reduced while recording U_z voltage signal. At a certain point, the gradient of the tip-sample interaction overcomes the normal spring constant of the cantilever and the tip *jumps into contact* (point b in Figure 2.5). When the tip is in contact with the sample surface, the vertical distance decreased even more causing an increase in the repulsive tip-sample interaction as defined by the linear region of

the purple curve in Figure 2.5. The slope of the linear region of the force-distance curve in conjunction with the normal spring constant of the cantilever allows determining θ_z . Once the tip-sample interaction reaches a certain level (point c in Figure 2.5), the tip is retracted from the surface and is subsequently *released* at an effectively attractive interaction force (point d in Figure 2.5). The magnitude of this attractive force is related to the *adhesion* that acts between the tip and the sample.

2.3 Measuring Lateral Forces via Friction Force Microscopy

As explained earlier, in 1987 Mate and co-workers have introduced a manifestation of conventional contact mode AFM used for detection of lateral interaction forces which is called the friction force microscopy (FFM) [6]. The principle of FFM is based on the fact that the PD can measure the torsional deflection of the cantilever during sample scanning due to lateral forces acting at the very apex of the tip (Figure 2.6) by simply tracking the “((A+C) - (B+D))” voltage signal.

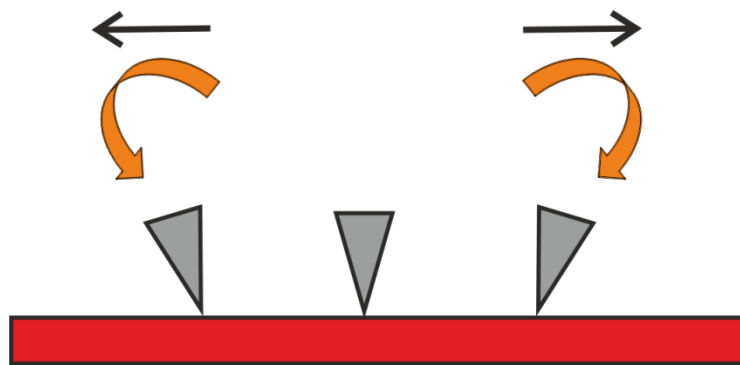


Figure 2.6 An illustration of torsional twisting undergone by the cantilever of the AFM during scanning to the left and right on a sample surface, respectively. The amount of twisting and the resulting change in the horizontal position of the laser spot on the PSPD are proportional to the lateral force, F_1 .

A practical problem associated with the detection of the lateral force signal during experiments is the fact that the reference horizontal position of the laser spot may drift with increasing normal force (and consequently the mean displacement of the piezoelectric tube in the z direction) due to cross-coupling between the channels. In order to overcome this problem, a method based on the idea of a “friction loop” formed by lateral force traces recorded during forward and backward scans is applied (Figure 2.7) [22]. Here, the half-width of the friction loop is taken to be equal to the friction force F_f acting between the tip and the sample.

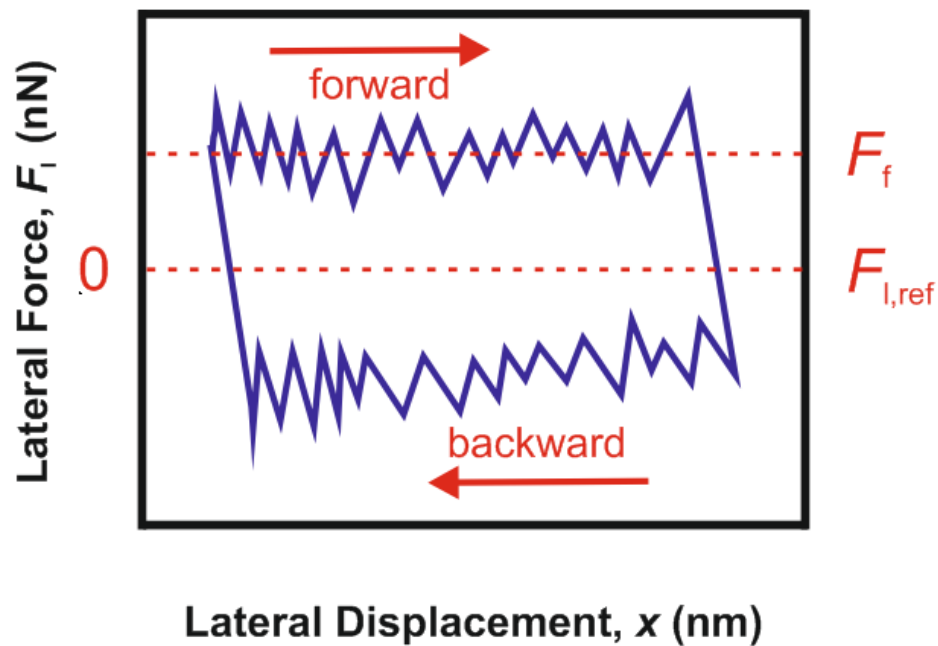


Figure 2.7 An example of a “friction loop” formed by lateral forces recorded during forward and backward scans (as indicated by red arrows) along the lateral x -axis. The reference lateral force value ($F_{l,ref}$) is taken to be equal to zero. The half-width of the loop gives the magnitude of the friction force. Please note that the inverse sign for the lateral force signals in the forward and backward directions due to cantilever twisting in inverse directions (see Figure 2.6).

Chapter 3

Selection of Materials: Gold on Graphite

3.1 Highly Oriented Pyrolytic Graphite: Structure and Physical Properties

Highly oriented pyrolytic graphite (HOPG) is a very commonly utilized material for all kinds of scanning probe microscopy (SPM) experiments, from scanning tunneling microscopy (STM) [23] to noncontact atomic force microscopy (NC-AFM) [24]. It is easily cleaned and prepared for high-resolution imaging by simple cleaving with scotch tape and remains clean even under ambient conditions for extended periods of time due to its chemical inertness. As such, it may be readily imaged with atomic resolution via STM under ambient conditions [23]. Moreover, the recently discovered capability to produce graphene via mechanical exfoliation has resulted in a renewed interest in the physical properties of this material [25].

HOPG is composed of individual monolayers of carbon atoms arranged in a honeycomb pattern (space group $P6_3/mmc$) and stacked on top of each other in the AB sequence [26]. In a single layer of graphite, which is also referred to as *graphene*, carbon atoms are bonded to each other by strong covalent bonds (sp^2 –

bonding) with a separation of $a_{\text{HOPG}} = 1.415 \text{ \AA}$. The *hollow* sites of the resulting honeycomb structure are separated by $b_{\text{HOPG}} = 2.46 \text{ \AA}$ (Figure 3.1(a)). Individual graphene layers are then stacked on top of each other in an AB sequence as shown in Figure 3.1(b), in which the separation distance between two graphene layers is seen to be $c_{\text{HOPG}} = 3.4 \text{ \AA}$. Individual graphene layers are interacting with each other via relatively weak van der Waals forces; hence, the bonding in an individual sheet is much stronger than the bonding among two sheets. As a result, this asymmetry in bonding strength leads to the ability to easily cleave HOPG so that individual layers of graphene are separated from the bulk graphite. This straightforward preparation results in atomically flat and clean surfaces ready to be investigated via SPM.

As HOPG is a well-known solid lubricant, its exceptional frictional properties have been the subject of nanotribology research in the past [29, 30]. Despite the fact that the physical reasons behind its frictional characteristics are still a matter of debate [27], HOPG has also been the substrate of choice for nanotribology experiments involving the lateral manipulation of antimony (Sb) and gold (Au) nanoparticles [13, 28]. The main advantages presented by HOPG for such experiments (some of which have been already mentioned) can be summarized as:

1. Atomically-flat, large terraces on the order of microns,
2. Ease of preparation
3. Chemical inertness

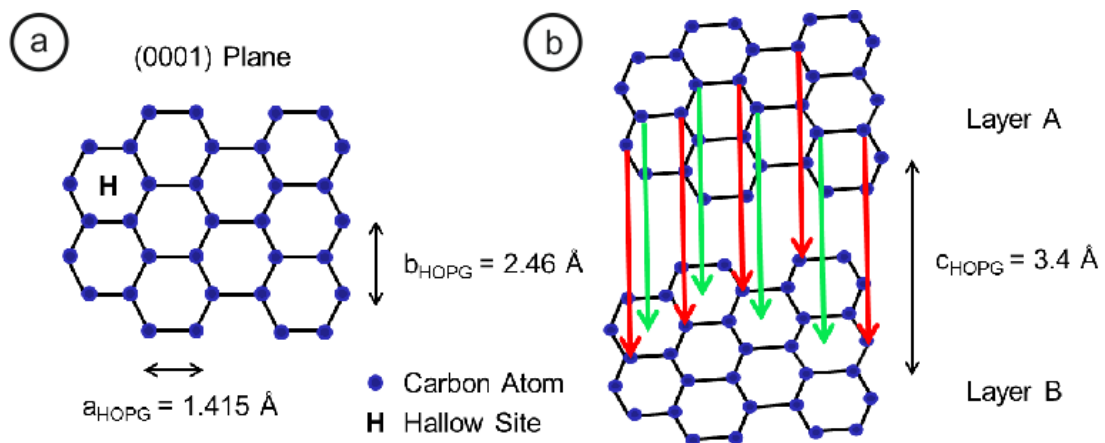


Figure 3.1 (a) A single graphene layer where the hollow sites and carbon atoms in the honeycomb structure are indicated. (b) Schematic describing the structure of bulk graphite. As one can infer from the drawing, half of the carbon atoms in the top layer have neighboring atoms in the bottom layer (shown with red arrows) whereas the other half do not (shown with green arrows).

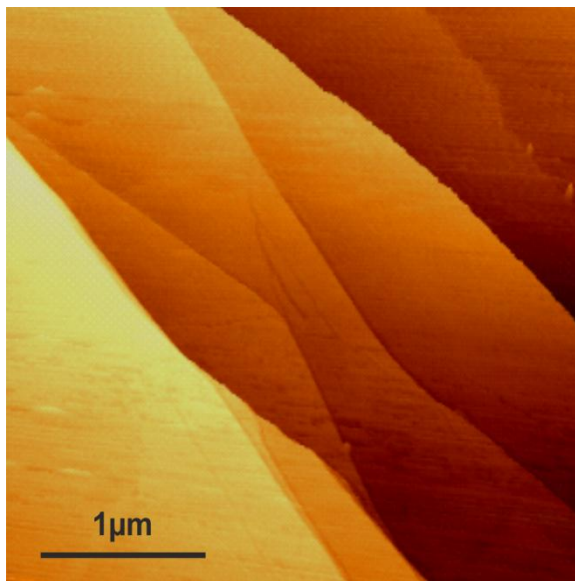


Figure 3.2 A typical topographical map of the HOPG (0001) surface recorded with contact mode AFM, showing large, flat terraces.

Bulk HOPG has polycrystalline structure and all layers are oriented in parallel along the [0001] direction (the *c*-axis) while the remaining axes have random distribution (*pyrolytic*). Each HOPG poly-crystal consists of microscopic mono-crystal grains in different sizes which are slightly disoriented and thus appears as a mosaic-like structure. This mosaic-like structure is caused by the angular spread of the *c*-axis inside the HOPG crystal. In order to characterize the deviation angle of the grain boundaries from the perpendicular *c*-axis, a measurement for the parallelism of grains, so called “mosaic spread”, can be applied. The lower the mosaic spread, the more highly ordered the HOPG and the higher the quality. This results in a reduction in the number of number of steps on a freshly cleaved HOPG surface with an increase in average terrace size (please see Figure 3.2 for a typical topographical map of the HOPG (0001) surface acquired via AFM). Please note that for the experiments reported in this thesis, HOPG samples of the highest commercially available quality have been used (Ted Pella Inc., USA, HOPG grade ZYA, 10 x 10 x 1.5 mm).

3.2 Gold: Structure and Physical Properties

Gold (chemical name Au, derived from the Latin name *aurum*) is the element with atomic number 79. Gold is a transition metal and is located in the 6th period and 11th group of the periodic table. Under standard conditions, gold is a solid, yellow-colored metal with the highest ductility and malleability among all other metals. The pure Au metal melts at 1063 °C and boils at 2966 °C. Its atomic weight is 196.967 with a density of 19.32 g/cm³ at 20 °C.

Gold crystallizes in the face-centered cubic (FCC) lattice structure with a lattice parameter of $a_{\text{Au}} = 4.08 \text{ \AA}$ (Figure 3.3(a)). The inter-atomic distance between the (111) planes is $c_{\text{Au}} = 2.36 \text{ \AA}$, as confirmed by the TEM image presented in Figure 3.3(b). Gold is also one of the most inert metals and does not oxidize under a wide

range of conditions. The fact that Au retains its crystalline structure in a very large size range and exhibits high chemical stability make it a very suitable candidate for nanotribology experiments performed via AFM under ambient conditions.

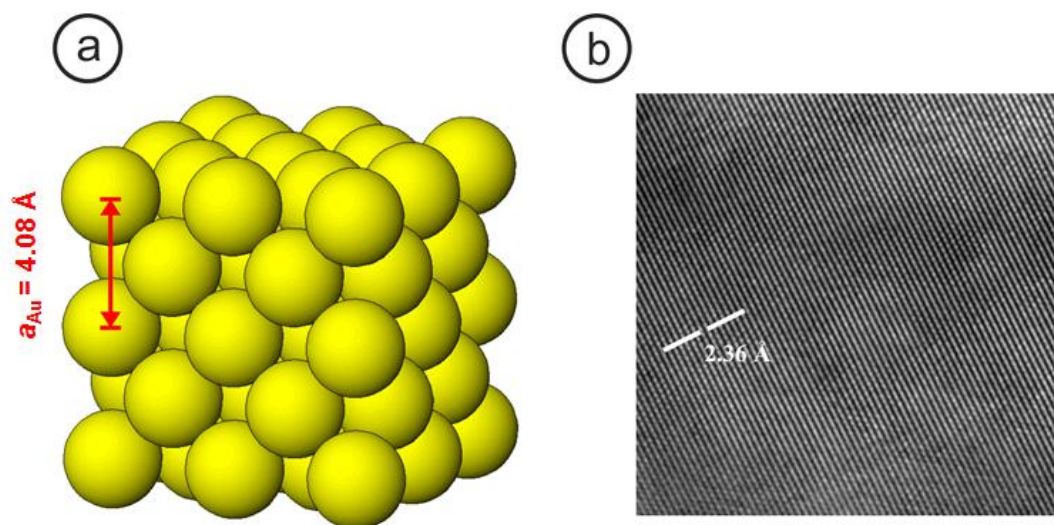


Figure 3.3 (a) FCC crystal structure of gold. Image taken from [31]. (b) A high-resolution, cross-sectional TEM image of a Au nanoparticle exhibiting (111) planes with inter-atomic distance of 2.36 \AA .

3.3 The Au/HOPG Material System

As mentioned previously in Chapter 1, if a block is slid over a macroscopically flat substrate, small asperities (usually not detected by the naked eye) caused by the roughness of the bottom surface of the block will have to overcome the small asperities associated with the substrate surface for the block to move in a given direction. The energy dissipated during this phenomenon can be interpreted as friction. The principle mechanism described for small asperities in this way is relevant for much smaller, atomically-flat and crystalline interfaces as well; but in a slightly different way: Now, individual atoms of the top surface need to overcome the potential energy barriers constituted by the bottom surface atoms for the top

surface to be able to laterally move from one location to another. If the two surfaces are *commensurate* (if they have the same atomic spacing), then they can periodically *lock* into each other, and under these circumstances, the energy needed to make the surfaces move would increase linearly with increasing number of atoms, as each individual atom of the top surface would have to overcome the same potential energy barrier that a single atom would encounter (Figure 3.4, left). On the other hand, if the two surfaces are *incommensurate* and exhibit different atomic spacing, then it is not possible for the atoms of the top surface to *fit* into the potential energy wells associated with the bottom surface. As such, the potential energy that each atom needs to overcome for lateral motion decreases with increasing number of atoms, resulting in a dramatic reduction in friction (Figure 3.4, right). This effect is called *structural lubricity* [30].

Based on this detailed explanation, one would expect that gold nanoparticles (AuNPs) should slide with very low friction on HOPG, due to the incommensurate crystal structures of Au and HOPG. Dietzel *et al.* have recently performed lateral manipulation experiments on this sample system under clean, ultrahigh vacuum (UHV) conditions and have indeed confirmed the occurrence of structurally lubric sliding [28]. Despite this fact, structural lubricity has not been observed yet for similar sample systems under ambient conditions, with the only exception of experimental results that are presented in Chapter 6 of this thesis.

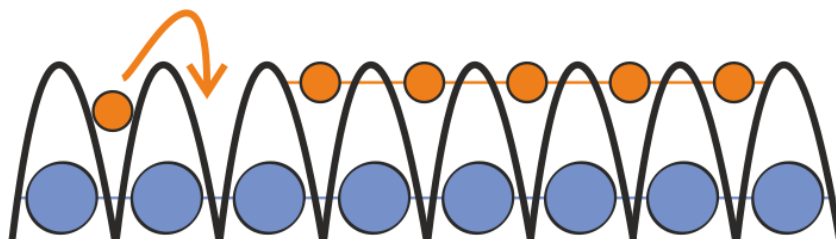


Figure 3.4 An illustration of the principle of structural lubricity. While the single orange atom on the left needs to overcome a large potential energy barrier to laterally move over the surface constituted by the blue atoms, the surface

consisting of orange atoms on the right experiences much smaller potential barriers due to structural incommensurability with the bottom surface.

Due to its potential promise for structurally lubric sliding under ambient conditions because of lattice mismatch, the Au/HOPG material system has been chosen for the nanotribology studies discussed in this thesis. While the details of sample preparation are explained in Chapter 4, Figure 3.5 provides an overview of the morphology of the material system, obtained (a) after thermal deposition of Au on HOPG and (b) after post-deposition thermal annealing. As one can infer from Figure 3.5(b), AuNPs with well-defined facets (thus crystalline) and of various size are obtained on HOPG via this procedure, validating its suitability for lateral nano-manipulation studies. Finally, it should be indicated that the particularly low surface energy of HOPG (0.07 J/m^2) [32] and the somewhat average surface energy of Au (1.5 J/m^2) [33] fundamentally results in a weak interaction (adhesion) of AuNPs on the HOPG, which is expected to increase the associated lateral mobility (Figure 3.6).

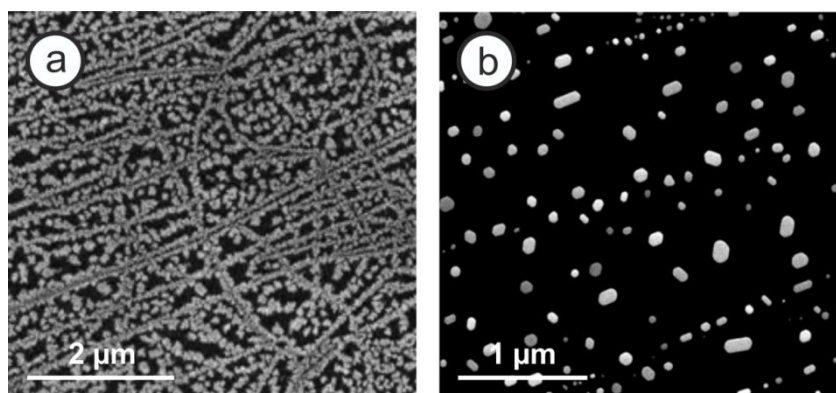


Figure 3.5 (a) SEM image of the HOPG substrate after thermal deposition of 1 \AA Au, resulting in a *channeled* thin film. (b) SEM image of the HOPG substrate decorated with crystalline AuNPs of various sizes after post-deposition annealing, ready for subsequent nanotribological investigation via AFM.

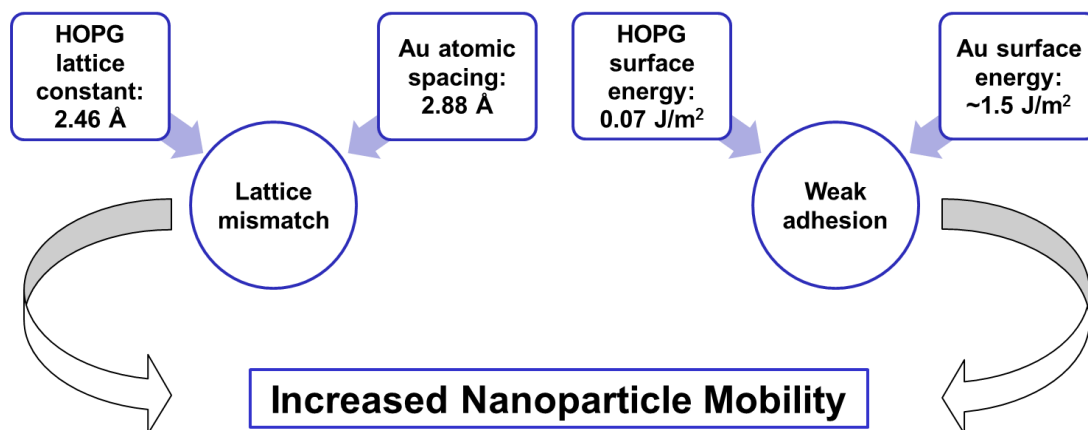


Figure 3.6 Schematic drawing emphasizing the suitability of the Au/HOPG material system for nano-manipulation experiments based on lattice mismatch and the particularly low surface energy of HOPG.

Chapter 4

Preparation and Structural Characterization of Gold Nanoparticles

4.1 Background

As indicated in previous chapters of this thesis, a material system consisting of gold nanoparticles (AuNP) thermally deposited on highly oriented pyrolytic graphite (HOPG) has been chosen for the nanotribological experiments to be conducted via AFM under ambient conditions, motivated by the fact that AuNPs should expose crystalline surfaces which will not oxidize over the course of several weeks. In this chapter, the preparation and structural characterization of the AuNP/HOPG material system will be discussed.

The growth kinetics of AuNPs on HOPG substrates have been extensively studied in the literature [34-38]. When gold is thermally deposited on air-cleaved graphite substrates at room temperature; small, branched and dispersed islands grow (Figure 4.1(a)). On the other hand; larger, dendritic gold islands structures are observed upon thermal deposition on vacuum-cleaved graphite, owing to increased surface cleanliness promoting increased island mobility and growth (Figure 4.1(b)) [34].

When the substrate temperature is increased from room temperature to 450 °C, three-dimensional gold nanoislands with well-defined facets appear (Figure 4.1(c,d)) as the gold atoms are now able to acquire thermal activation energies necessary to grow along preferred crystallographic directions, within the framework of a kinetically-controlled growth mechanism [34]. This results consequently in lower surface coverage.

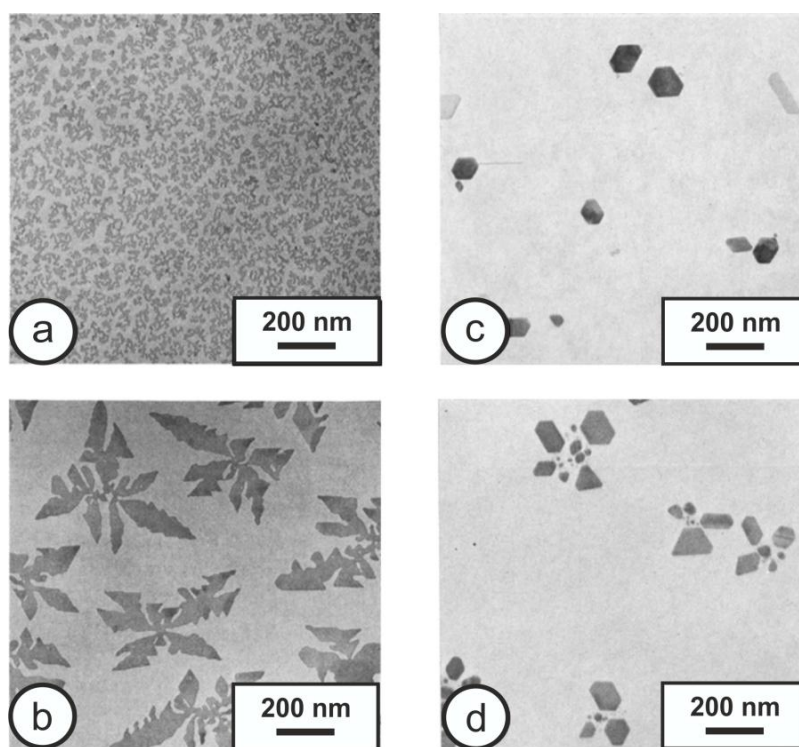


Figure 4.1 (a) Au film deposited on air-cleaved graphite at room temperature, 9.9 Å, (b) Au film deposited on vacuum-cleaved graphite at room temperature, 9.9 Å, (c) Au film deposited on air-cleaved graphite at 450 °C, 168 Å, (d) Au film deposited on vacuum-cleaved graphite at 450 °C, 168 Å.

It should be indicated that the energy barrier for surface diffusion of gold atoms on HOPG is less than 24 meV [36], which promotes rapid island growth and coalescence. The morphology of large, well-faceted and separated Au islands

acquired at elevated temperatures is supported by the existence of relatively long diffusion lengths of Au atoms on HOPG [38]. Additionally, it should be pointed out that well-faceted AuNPs as seen in Figure 4(c,d) mostly grow with (111) and (100) side facets on HOPG [37].

In the absence of the capability to change the substrate temperature during thermal evaporation of gold on graphite, different strategies may be employed to obtain well-faceted and relatively large AuNPs with sufficient separation from each other suitable for subsequent nano-manipulation studies. One such approach which has recently been tried on graphene involves post-deposition annealing [39] which we have also employed in our work, as explained in Section 4.3.

4.2 Thermal Evaporation

4.2.1 Basic Principle and Experimental Parameters

Thermal evaporation is one of the most frequently employed physical vapor deposition (PVD) techniques, where the material to be evaporated and eventually deposited is loaded into a metal crucible that is subsequently introduced into a high vacuum (HV) chamber. The crucible is mostly made of tungsten or tantalum, metals with very high melting points. As the crucible is heated inside the HV chamber, the material inside starts to melt and then evaporate, resulting in atoms being ejected towards the substrate surface.

As the first step in sample preparation, high-quality (Ted Pella, ZYA grade) HOPG substrates have been mechanically cleaved in air via scotch tape and immediately transferred into the HV chamber of the thermal evaporation system (Vaksis PVD Vapor – 3S, Figure 4.2) available in the clean room facility of the National Nanotechnology Research Center (UNAM).



Figure 4.2 Thermal Evaporator, Vaksis PVD Vapor – 3S. Picture taken from [40].

As the evaporation material, 999.9 purity gold has been employed (Vakıf Bank). Evaporation onto the HOPG substrate took place at a deposition rate of 0.1 \AA/s and a base pressure on the order of $5 \times 10^{-6} \text{ Torr}$. During deposition, the HOPG substrate was held at room temperature as the equipment utilized for the experiments does not currently allow changing the substrate temperature. The parameters used for the Au deposition are summarized in Table 4.1.

Table 4.1. Physical vapor deposition parameters of the Au deposition.

Material	Density (g/cm³)	Tooling Factor
Gold	19.3	52%

4.2.2 Effect of Deposition Amount on Thin Film Morphology

In order to obtain a heterogeneous sample system which is suitable for nanotribological investigation via AFM consisting of individual AuNPs with well-defined shapes and reasonable lateral separations on HOPG, the first preparation step involves the thermal evaporation of Au on freshly cleaved HOPG, as indicated in the previous section. Due to the relatively low surface energy of the HOPG substrate and the resulting increase in mobility of Au atoms on this substrate, non-uniform surface coverage of Au on HOPG has been observed in the past, especially at low deposition amounts [34-38]. Taking previous studies in the literature into account, we have further investigated in this thesis different deposition amounts to examine how the surface coverage of Au and the morphology of the resulting thin films are affected by this experimental parameter [41].

To observe the coverage and morphology of Au thin films on HOPG, scanning electron microscopy (SEM) has been utilized. SEM is the most commonly utilized electron microscopy technique in which an electron beam accelerated with high voltages (typically 5 kV and above) scans over the sample surface of interest. Information about the morphology and composition of the sample surface is obtained by detecting electrons deflected and/or ejected from the atoms on the sample surface and a certain distance below. In order to investigate the morphology and distribution of AuNPs on HOPG, samples have been analyzed via the SEM instrument available in UNAM (FEI Quanta 200 FEG, typically operated at 10 kV, see Figure 4.3).

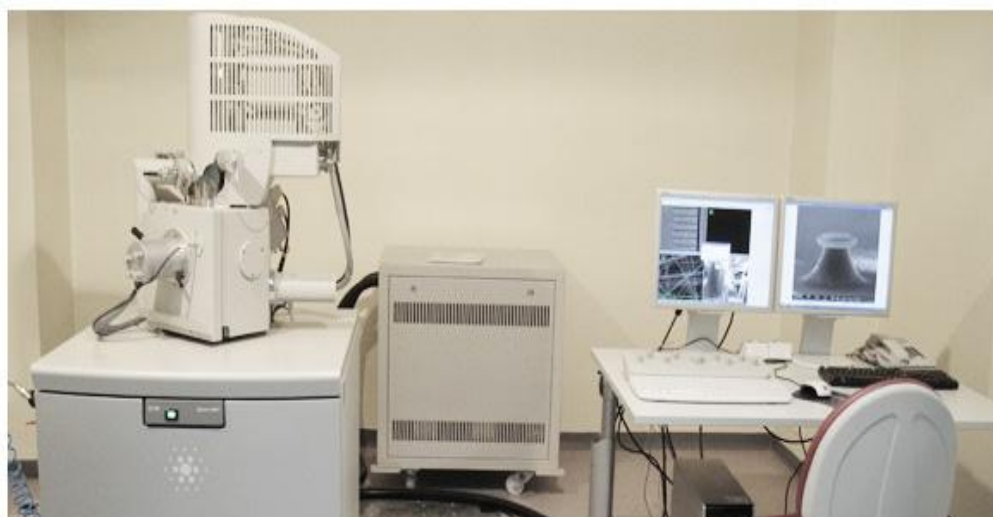


Figure 4.3 The SEM instrument used for the experiments presented in this thesis (FEI Quanta 200 FEG). Picture taken from [42].

Figure 4.4 shows the effect of deposition amount on the resulting thin film morphology for total deposition amounts of 20 Å, 10 Å, 5 Å and 1 Å via SEM images. Thin film morphologies at low coverages comprise inter-connected, non-uniformly dispersed and irregularly-shaped gold islands. Starting from a thickness of 20 Å, close to full surface coverage is observed (Figure 4.3(a)). The surface coverage and average island size gradually drop with smaller deposition amounts (Figure 4.3(b,c)), until uncovered regions of the substrate on the order of several hundreds of nm become observable at a deposition amount of 1 Å as seen in Figure 4.3(d). The fact that an aggregation of Au islands along linear features on the HOPG substrates becomes perceivable at small deposition amounts such as 1 Å promotes the argument that nucleation and growth primarily takes place at surface defects such as step edges and grain boundaries, in accordance with the literature [38].

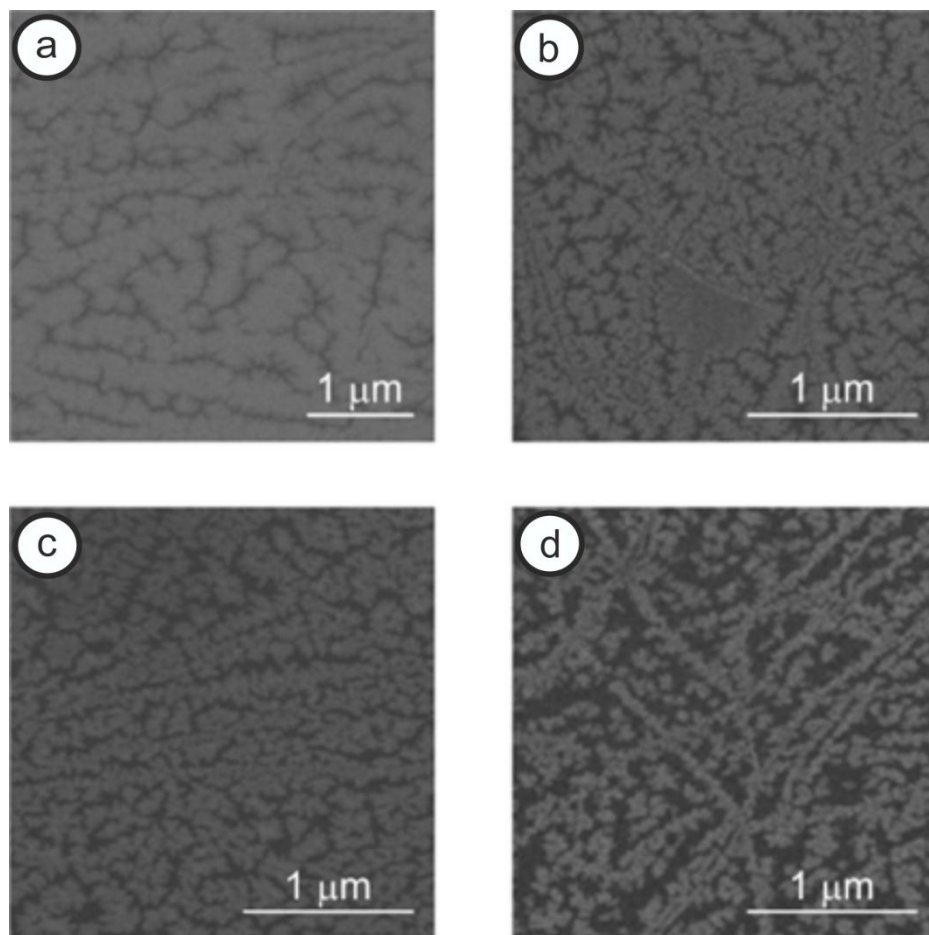


Figure 4.4 SEM images of as-deposited Au thin films on HOPG for total deposition amounts of 20 Å (a), 10 Å (b), 5 Å (c) and 1 Å (d).

The coverage of the HOPG substrate by Au as a function of film thickness has also been investigated as shown in Figure 4.4 [41]. These results are in line with the *dynamic scaling theory of growing interfaces*, involving four stages that can be summarized as nucleation, lateral growth, coalescence and vertical growth; leading to an Avrami-type relationship between surface coverage and film thickness, which is characterized by rapid lateral growth at low coverages, followed by a damped coverage rate with increasing film thickness. The result presented in Figure 4.5 confirms this scenario that corresponds to a lateral growth and surface-diffusion-

driven coalescence process, based on the relatively weak chemical interactions between the adsorbed Au atoms and the HOPG surface [43].

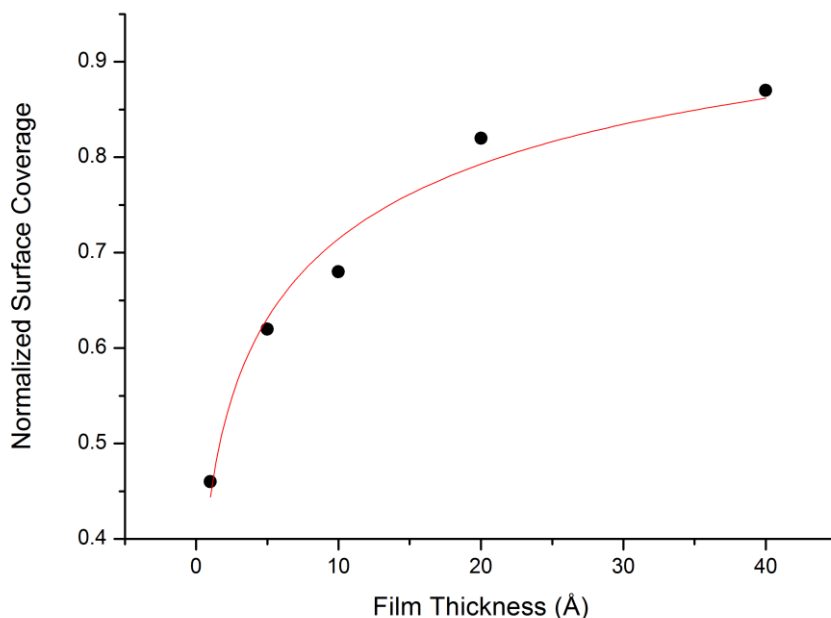


Figure 4.5 Surface coverage of Au on HOPG as a function of film thickness. An Avrami-type fit represented by the red solid curve reasonably describes film growth [43].

4.3 Formation of AuNPs by Post-Deposition Annealing

While the SEM results provided in the previous section provides beneficial information about the surface coverage and morphology of Au thin films on HOPG as a function of deposition amount, the resulting material system is impractical for nanotribological investigation via AFM because of a lack of structurally well-defined (faceted) AuNPs at reasonably large separations. In order to transform the deposited Au films into well-faceted and reasonably large (few 100's of nm

laterally) AuNPs, post-deposition annealing has been performed in a quartz furnace (Alser Teknik/ProTherm) located in UNAM (Figure 4.6).



Figure 4.6 Quartz tube furnace used for post-deposition annealing. Image taken from [44].

Post-deposition annealing at temperatures ranging from 400° C to 650° C and for annealing times on the order of 30 min. to 4 h has been performed, under atmospheric pressure. Based on results of thermal evaporation experiments, samples comprising 1 Å of deposited Au on HOPG have been chosen for post-deposition annealing due to the low surface coverage.

Figure 4.7 summarizes the results of post-deposition annealing in the quartz furnace [41]. A significant effect on the morphology and distribution of AuNPs on HOPG can be easily distinguished from SEM micrographs. As annealing temperatures and times increase, an obvious reduction of surface coverage and eventual formation of large, coalesced AuNPs with well-defined facets takes place. While annealing temperatures up to 500° C only results in non-faceted, irregularly-

shaped Au islands as demonstrated in Figure 4.6(a), well-faceted, hexagonal or elongated-hexagonal AuNPs are observed at annealing temperatures of 600-650 °C (Figure 4.6(b-d)), in accordance with a recent annealing study performed on Au thin films on single- and few-layer graphene [39]. To sum up, the experimental results presented here constitute an alternative process used to obtain well-faceted AuNPs on the HOPG substrate, in the absence of the capability to change substrate temperatures during deposition.

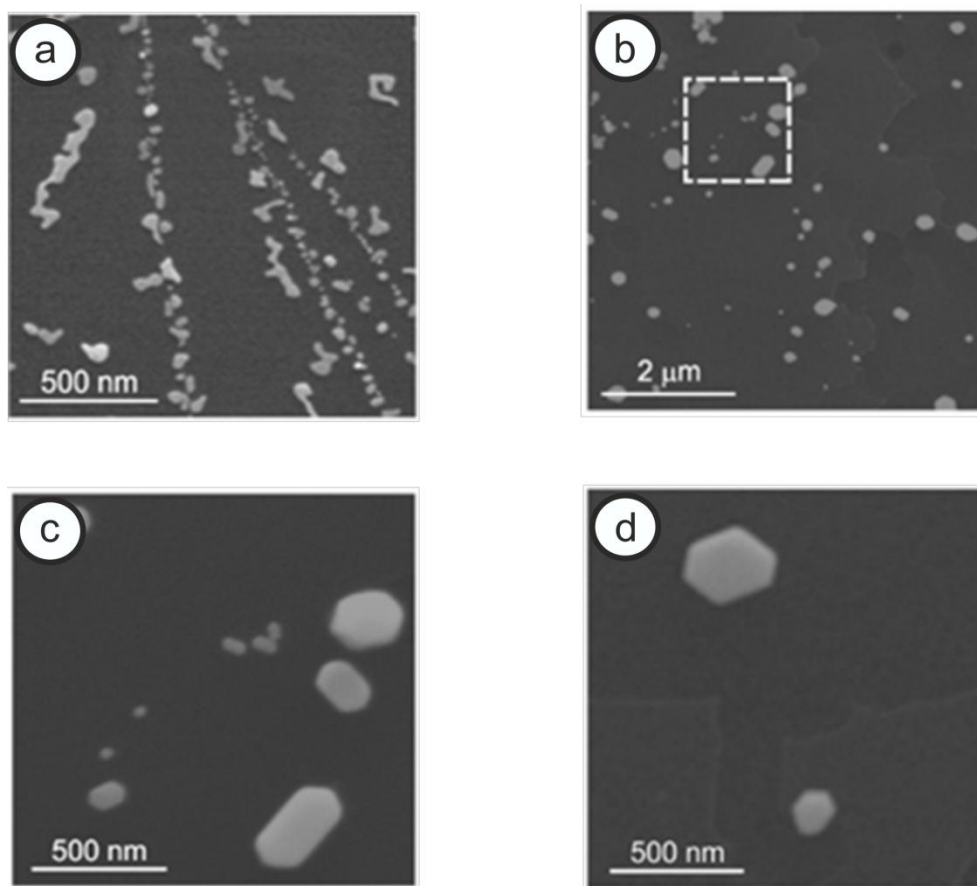


Figure 4.7 SEM images of the AuNP/HOPG material system after post-deposition annealing in quartz furnace at (a) 500 °C for 30 min., (b, c) 600 °C for 2 h and (d) 650 °C for 2 h.

4.4 Structural Characterization of AuNPs

4.4.1 Determination of AuNP Size Distribution via Scanning Electron Microscopy

As explained in the previous section, well-defined (faceted) AuNPs at reasonably large separations from each other on the HOPG substrate are required for precise nanotribological characterization via AFM. As such, in order to get a clear picture about the resulting material system, we have investigated the lateral size distribution of hexagonal/elongated-hexagonal AuNPs obtained after post-deposition annealing [41], results of which are presented in Figure 4.8. A relatively wide distribution of AuNP sizes up to 500 nm with a mean particle size of 168 ± 106 nm are obtained after our sample preparation procedure. Let us finally indicate that the wide distribution of AuNP lateral size is favorable for nanotribological investigations, as it leads to the opportunity of performing nano-manipulation experiments where interfacial friction forces acting on AuNPs of different size shall be quantified, as discussed in Chapter 6 of this thesis.

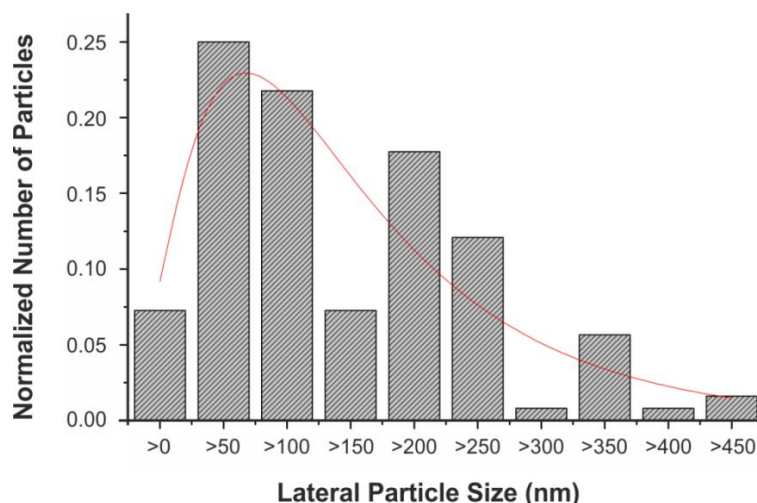


Figure 4.8 AuNP size distribution after post-deposition annealing at 600-650 °C. Lateral particle sizes up to 500 nm are observed. The solid red curve is a fit by the *log-normal* function [43].

4.4.2 Confirmation of AuNP Crystallinity via Transmission Electron Microscopy

Numerous studies have evidenced up to the present that friction experienced by two bodies in contact is mainly related to the structure of the interface [13, 28, 45]. In this respect, well-defined (crystalline) surfaces are essential to precisely investigate the influence of interface structure on friction at the nanoscale. In other words, AuNP/HOPG presents a suitable material system for nano-manipulation experiments since the crystallinity of the Au-HOPG interface should be conserved even under ambient conditions.

In order to confirm the crystalline character of thermally deposited and post-deposition annealed AuNPs on HOPG to be used in our nanotribology experiments, transmission electron microscopy (TEM) has been utilized [41]. TEM is a very high-resolution (down to the level of individual atoms) electron microscopy technique that involves passing a high-energy (typically above 100 kV) electron beam through an ultra-thin specimen and recording the changes induced in the beam by its interaction with the sample with a detector located on the other side. The TEM instrument used in our experiments (FEI Tecnai G2 F30, typically operated at 300 kV) is located in UNAM (Figure 4.9).

The TEM samples have been prepared in two ways:

1. To investigate individual AuNPs, a thin layer of the Au-covered HOPG sample has been mechanically peeled off and subsequently sonicated in ethanol, which was followed by drop-casting on a Cu grid (300 mesh).
2. For cross-sectional TEM imaging, required to confirm crystalline orientation and the absence of an oxide layer, TEM samples are prepared via focused ion beam (FIB) milling (FEI Nova 600 Nanolab) (Figure 4.10). Initially, a region of the sample containing several AuNPs is coated with

epoxy to protect the surface during ion milling and then, a thin lamella is carved via ion beam. The cut lamella is tilted for pre-thinning; the final, fine thinning is applied at lower ion beam energy. Finally, in order to place the resulting sample to the TEM grid, it is glued via Pt metal by welding to the FIB support.

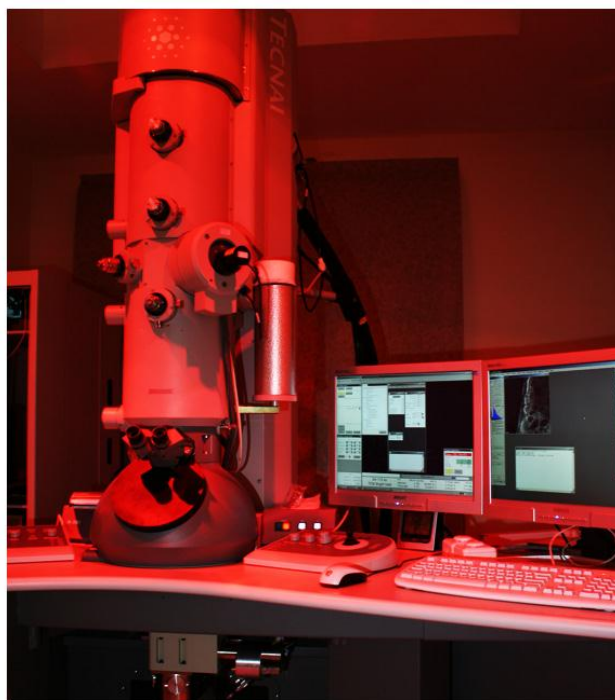


Figure 4.9 The TEM instrument used for the experiments presented in this thesis (FEI Tecnai G2 F30). Picture taken from [46].



Figure 4.10 The FIB instrument used for the experiments presented in this thesis (FEI Nova 600i Nanolab). Picture taken from [47].

Figure 4.11(a) displays a top-view TEM image of an individual AuNP with well-defined facets whereas Figure 4.11(b) depicts a high-resolution TEM (HR-TEM) micrograph recorded at the edge of the hexagonal AuNP which reveals the crystalline order of Au atoms. The electron diffraction pattern presented in Figure 4.11(c) provides further confirmation for the crystalline structure of the AuNP. Finally, the cross-sectional, high-resolution TEM image in Figure 4.11(d) reveals in high detail the crystalline structure of the AuNP, all the way to the very edge, proving that the AuNP is not oxidized on its surface and thus is suitable for, *e.g.*, studies of structural lubricity. Please note that since the particular AuNP imaged in Figure 4.11(d) has been exposed to ambient conditions for several weeks, the possibility for the formation of an oxide layer on AuNPs during extended periods can thus be excluded.

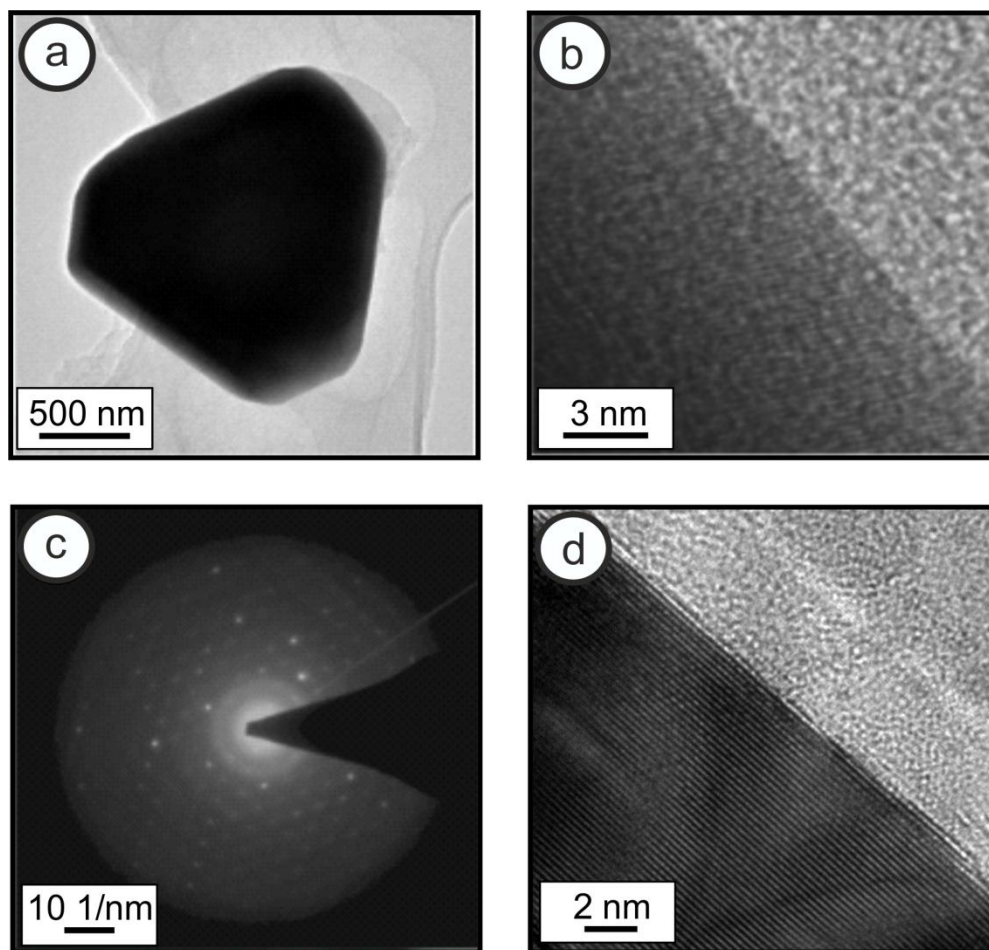


Figure 4.11 (a) TEM measurements performed on a single, well-faceted AuNP, (b) high resolution image at the edge of the AuNP, (c) associated electron diffraction pattern. (d) Cross-sectional, high-resolution TEM image clearly demonstrating crystalline order and the absence of an oxide layer on the AuNPs.

4.4.3 Topographical Characterization of AuNPs via Contact Mode AFM

In addition to SEM and TEM measurements, AFM experiments have been carried out to topographically characterize AuNPs distributed on the HOPG substrate [41]. A commercial AFM instrument (PSIA XE-100E) shown in Figure 4.12 has been operated under ambient conditions and contact mode imaging has been mainly

utilized to measure the topography of the sample surface. Silicon cantilevers (for contact mode cantilevers: Nanosensors PPP-CONTR series, radius of curvature ≈ 10 nm) have been preferred for all AFM measurements and calibrated according to the method reported by Sader et al. [48] to determine normal spring constants.

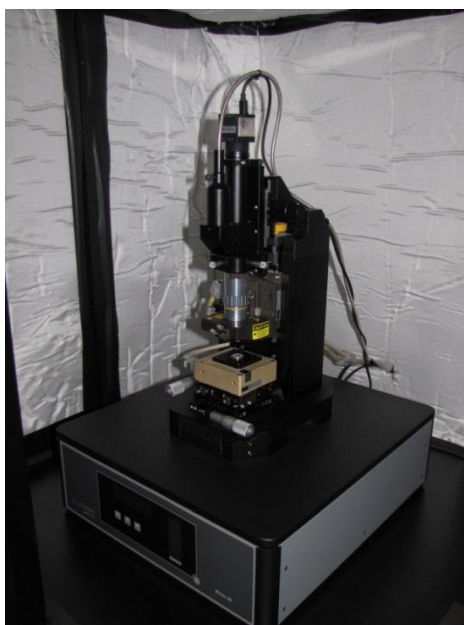


Figure 4.12 The AFM instrument used for the experiments presented in this thesis (PSIA XE-100E). Picture taken from [49].

Contact mode AFM at low applied loads (*i.e.*, set points or normal forces, < 1 nN) has been performed to image the topography associated with post-deposition annealed AuNP/HOPG samples. The AFM imaging has revealed that most AuNPs are trapped between the step edges of the HOPG substrate, presumably due to the increased mobility experienced by the AuNPs during annealing (see the black, dashed rectangle in Figure 4.13(a)). On the other hand, AuNPs not trapped between step edges and located on HOPG terraces in an unobstructed fashion were easily and unintentionally manipulated by the AFM tip during raster-scanning, despite the low magnitude of normal forces applied to the surface (see the blue, dashed rectangle in Figure 4.13(a)). While this observation provides certain hints towards

the occurrence of structurally lubric sliding for this sample system (which will be further investigated in Chapter 6), for the moment, focus will be placed on the structural and eventually, nanotribological characterization of immobile AuNPs stuck between HOPG steps, such as those seen in Figure 4.13(b).

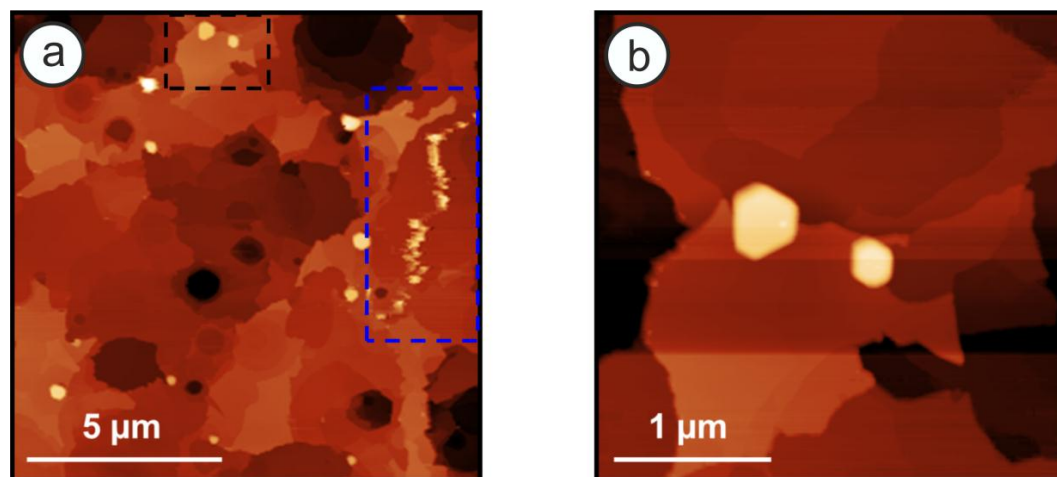


Figure 4.13 (a) Large scale contact mode AFM topography image of the AuNP/HOPG system, exhibiting immobile AuNPs (black, dashed rectangle) as well as an unintentional manipulation event (blue, dashed rectangle). (b) Contact mode AFM topography image of two AuNPs stuck between HOPG step edges.

Figure 4.14 illustrates a contact-mode topography image of a single, hexagon-shaped AuNP, as well as its three-dimensional representation. While the nanoparticle investigated here possesses a height of ~ 75 nm, AuNPs of 50 to 180 nm height have been observed during the experiments. It should be specified here that topography images of certain AuNPs bring out the presence of small round mounds on the top surface of AuNPs (usually ~ 10 nm across and < 10 nm in height) as highlighted in Figure 4.14(a). It is predicted that these small structures are produced during post-deposition annealing, even though the determination of the exact mechanism responsible is beyond the scope of this thesis.

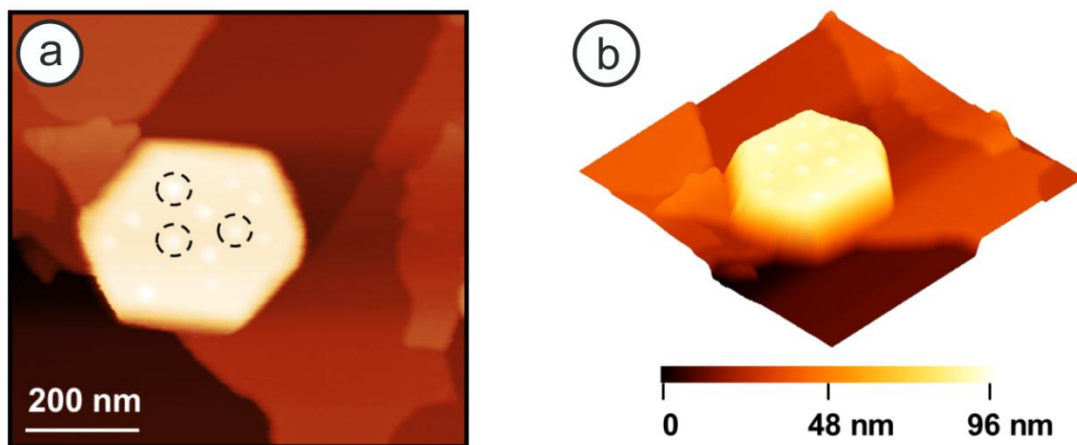


Figure 4.14 (a) Topographical map of a ~ 75 nm high AuNP trapped between HOPG steps acquired via contact-mode AFM, and (b) its 3D representation.

Chapter 5

Frictional Characterization of the AuNP/HOPG Material System

5.1 Background

As explained in the introduction chapter of this thesis, the single-asperity nature of the contact formed between the probe tip and the sample surface during AFM-based nanotribology experiments has allowed the detailed study of friction as a function of, *e.g.*, normal load, sliding velocity and temperature on the nanoscale in the last couple of decades [30, 50, 51] and has led to the observation and quantification of fundamental phenomena of importance such as *stick-slip* [10] and *superlubricity* [11].

Within this context, nanoparticles on flat substrates such as HOPG and mica [52, 53] are of particular interest, primarily due to the fact that they readily present a heterogeneous sample surface where the effect of changing experimental parameters such as normal load on frictional behavior can be compared and contrasted on the nanoparticles themselves and the substrates. Additionally, the recently increased interest in lateral manipulation experiments involving such

material systems [12] has led to the need of a comprehensive characterization of associated nanotribological properties.

It is interesting to note that very few experimental studies about the nanotribological properties of metallic surfaces have been reported in the literature [54-57]. In particular, Au(111) surfaces have been found to present very low friction at small applied loads under UHV conditions, while a substantial increase in friction accompanied by wear takes place at higher normal loads [54]. Furthermore, Au(111) surfaces submerged in ionic liquids have been shown to exhibit switchable frictional properties based on the application of an electrical potential [57]. On the other hand, an extensive analysis of nanoscale frictional properties of gold nanoparticles thermally evaporated on HOPG – the material system discussed in this thesis – has not been performed so far under ambient conditions.

Motivated by the background discussion above, a comprehensive nanotribological analysis of the AuNP/HOPG material system under ambient conditions performed by contact-mode AFM/FFM is presented in this chapter. Specifically, the calibration of relevant parameters for normal and lateral force sensing is discussed first, followed by a detailed characterization of friction as a function of normal load on the AuNPs themselves and the HOPG substrate. The chapter is concluded by an investigation of the increase in friction experienced at AuNP edges as a function of normal load and edge height, as well as a characterization of adhesion on AuNPs.

5.2 Force Sensor Calibration

5.2.1 Normal Spring Constant Calibration

To reliably determine the normal forces acting on between the probe and the sample surface during contact-mode AFM measurements, identification of the normal spring constant of AFM cantilevers utilized in the experiments is a required first step.

Numerous methods aimed to precisely determine the normal spring constant of AFM cantilevers have been reported in the literature [48, 58-61]. Among these calibration techniques, the two methods described by Sader *et al.* [48, 61] are widely applied due to their simplicity and robustness. As such the first calibration method put forward by Sader *et al.* [61] has been applied to determine the normal spring constant of AFM cantilevers used in this thesis.

This method is primarily based on the determination of the resonance frequency of the cantilever and the connection between mass, spring constant and resonance frequency. The mass of the cantilever is practically predicted from the dimensions of the cantilever, taking into account the density of the material from which it is made. Thus, for a rectangular cantilever, the normal spring constant is obtained by

$$k = M_e \rho_c b h L w_{vac}^2 \quad (5.1)$$

where w_{vac} is the angular resonance frequency of the cantilever in vacuum; h , b , and L are the thickness, width, and length of the cantilever, respectively; ρ_c is the density of the cantilever, and M_e is the normalized effective mass which solely depends on the aspect ratio of the cantilever.

Within the scope of this theory, the normal spring constant of the Si cantilever used in our experiments (a single Si cantilever has been employed for all experiments presented in this chapter for consistency) has been calculated as 0.23 N/m based on

the following data presented in Table 5.1. Please note that the resonance frequency is measure in air (w_{air}) rather than vacuum as the experiments are performed under ambient conditions. Furthermore, the normalized effective mass (M_e) has been taken as 0.2427 based on the fact that the value of the aspect ratio (L/b) of the cantilever is greater than 5 [61].

Table 5.1. Physical properties of the Si cantilever used in the FFM experiments

Thickness (μm)	Width (μm)	Length (μm)	Density (Si) (g/cm^3)	Resonance Frequency (kHz)	Angular Resonance Frequency (rad/s)
2	50	450	2.329	15.0	94,247

Since our experiments are performed under ambient conditions, the last point about the calibration of normal spring constant that needs to be emphasized is the shift in the resonance frequency caused by air damping. According to Sader *et al.* [61], the resonance frequency for a typical rectangular cantilever increases about 2% in vacuum and therefore, a 2% loss of resonant frequency has been taken into account in our calculations.

5.2.2 Lateral Force Calibration

Subsequent to the determination of the normal spring constant, the cantilever has to be calibrated in terms of the lateral force signal allowing the reliable quantification of the lateral forces recorded during AFM measurements.

In order to calibrate the lateral force signal provided by an AFM cantilever, the method reported by Varenberg *et al.* [62], sometimes referred to as the improved form of the *wedge method* put forward by Ogletree *et al.* [63], has been utilized in this thesis. The improved wedge calibration method involves the determination of

the forward and backward lateral force signals (see Chapter 2) on both sloped and flat facets of a standard calibration grating (TGF11 series by MikroMasch) with known dimensions and slope angles (Figure 5.1).

The details of the calibration procedure are quite involved and thus are not mentioned here; however the interested reader is referred to Refs. [62, 63] for further information. It should be indicated that the lateral force calibration factor α for the cantilever used in the experiments described in this chapter has been found to be 16 nN/V.

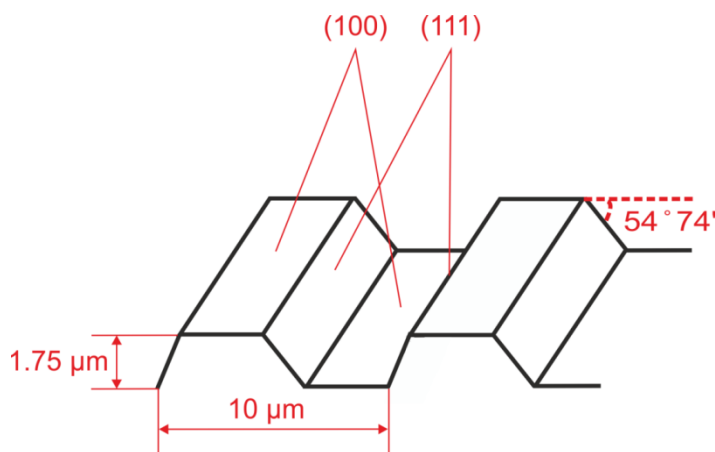


Figure 5.1 Schematic diagram of TGF11 silicon calibration grating. Relevant dimensions and crystallographic plane orientations are indicated.

5.3 Lateral Force Measurements on the AuNP/HOPG Material System

Based on the fact that sliding components featured in both micro/nano- and macro-scale functional devices are typically used under ambient conditions, it is of high importance that the nanotribological characteristics of related material systems are quantified in detail not only under UHV but also under operating conditions (*i.e.* in ambient).

In order to carry out associated studies, the AuNP/HOPG material system, the synthesis and structural characterization of which has been described in Chapter 4, is now nanotribologically analyzed via contact-mode AFM as illustrated in Figure 5.2. During all AFM measurements, a single AFM tip which is calibrated with respect to the steps described in Section 5.2 has been used to scan over the HOPG substrate on which the AuNPs are situated.

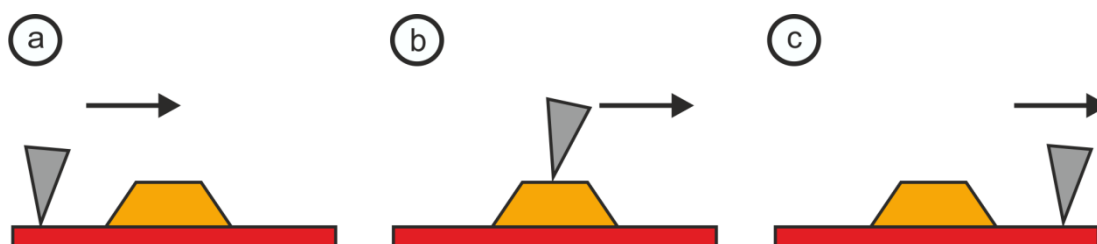


Figure 5.2 Illustration of the AFM tip scanning the AuNP/HOPG material system in contact mode. (a) AFM tip approaches the AuNP, (b) AFM tip is on the AuNP, (c) AFM tip leaves the NP behind and continues scanning on the HOPG substrate.

Based on the observation that most AuNPs on the HOPG substrate are manipulated laterally by the AFM tip even under low applied loads (see Chapter 4), efforts have been first directed to characterize the nanotribological properties of individual AuNPs trapped between the step edges of the HOPG substrate. Please note that lateral manipulation experiments are discussed in Chapter 6 of this thesis.

In order to nanotribologically characterize the AuNP/HOPG material system, lateral forces emerging between the AFM tip and the sample surface during contact-mode imaging have been recorded. Figure 5.3 shows a representative, large-scale lateral force map of the AuNP/HOPG material system with several AuNPs stuck between the step edges of HOPG substrate. It is observed that AuNP surfaces exhibit greater friction values than the HOPG substrate.

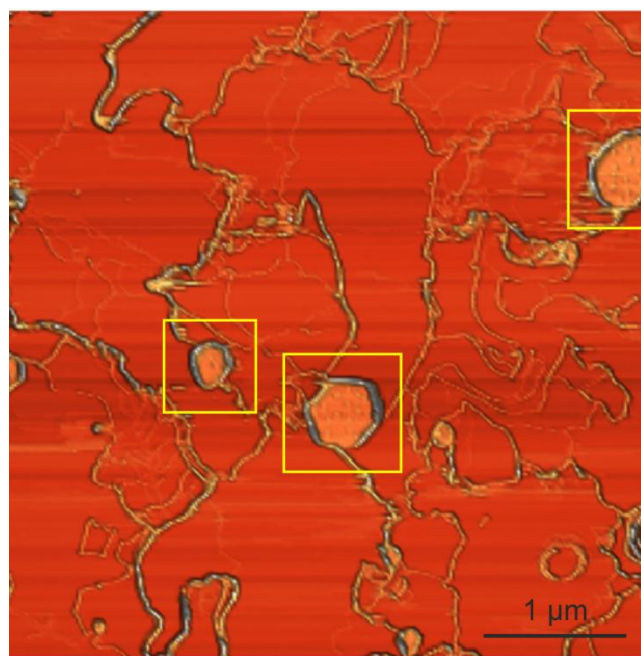


Figure 5.3 A representative, large-scale lateral force map of the AuNP/HOPG material system. AuNPs stuck between the step edges of HOPG substrate are highlighted. Lighter colors indicate higher friction forces.

A smaller lateral force map recorded at a region of the sample surface containing a single hexagonal AuNP stuck between the step edges of HOPG (acquired at a constant normal load F_n of 2.3 nN) is seen in Figure 5.4. As one can infer from the quantification of the lateral force signal along the black dashed arrow, the HOPG substrate exhibits vanishingly small (tens of pN) friction forces (F_f) while higher friction forces (0.60 nN) have been measured on top of the AuNP. Besides, a sudden increase in the lateral force (~ 2.5 nN) at the edge of the 50 nm high AuNP is seen. This abrupt raise is caused by the so-called *ratchet effect* and additional torsion (twisting) of the cantilever due to the *collision* during scanning caused by the height difference between the top surface of the AuNP and the HOPG substrate [64]. A quantification of this increase in friction at AuNP edges as a function of normal load and edge height is presented in the following sections of this chapter.

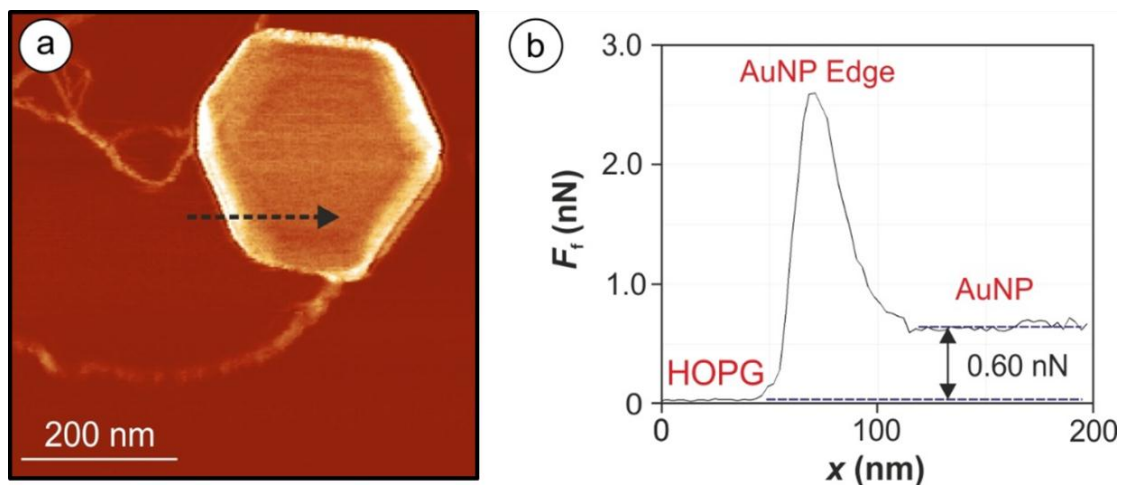


Figure 5.4 (a) Friction force map recorded on a region of the sample surface containing a hexagonal AuNP stuck between the step edges of HOPG, (b) The friction force profile along the dashed black arrow in (a). Image taken from [41].

5.3.1 Dependence of Lateral Force on Normal Load for AuNPs and HOPG

Acquiring a complete understanding of the physical principles which govern friction at the nanoscale is a continuing endeavor for scientists from various disciplines since the establishment of the nanotribology research field as it is thought that discovering the frictional behavior of macro-scale (multi-asperity) contacts can be achieved by understanding the physical principles for friction at nanoscale contacts. Within this regard, the dependence of friction force (F_f) on normal load (F_n) is of special concern. Previously, there have been reports of linear dependence of F_f on F_n [65] during FFM experiments, whereas various other FFM measurements have evidenced a specific relation between the two observables ($F_f \sim F_n^{2/3}$), confirming the assumption of a constant shear stress ($\tau = F_f/A$) and the validity of a Hertzian contact mechanics approach [65-69].

In order to make a fresh contribution to the previously reported experimental work involving the determination of friction principles at single asperities under ambient

conditions, an extensive nanotribological characterization of 20 separate AuNPs on the HOPG substrate has been performed within the framework of this thesis, focusing on a determination of the dependence of F_f on F_n . The results of this investigation are summarized in Figure 5.5. It is seen that a “2/3” power law within the error bars of our measurements is exhibited by AuNPs under ambient conditions (error bars for the friction force values on AuNPs have been calculated based upon measurements carried out on 20 separate AuNPs with the same cantilever on separate days). These results are compatible with the assumption of a constant shear stress and the validity of a Hertzian contact mechanics approach, as described below. Another point worth emphasizing is the presence of a non-zero friction force ($0.37 \text{ nN} \pm 0.11 \text{ nN}$) at zero normal load. The physical reason for this observation is the finite adhesion force formed between the tip apex and sample surface under ambient conditions because of the presence of a water meniscus at the contact. As such, the normal load and consequently, friction force, would become zero only at an effectively negative normal load (-1.80 nN). This force is equal in magnitude to the applied *pull-off force* which is essential to overcome the adhesion force and release the tip from the sample surface. To confirm the validity of the adhesion force predicted here, force-distance spectroscopy measurements have been performed to determine the magnitude of the required pull-off force, as presented in Section 5.4. It should be finally noted that, as expected from Figure 5.4, the F_f values measured on HOPG are much smaller than the AuNPs, due to the outstanding lubrication properties of this material. Consequently, the functional form of the dependence of F_f on F_n on the HOPG substrate is not straightforward to determine.

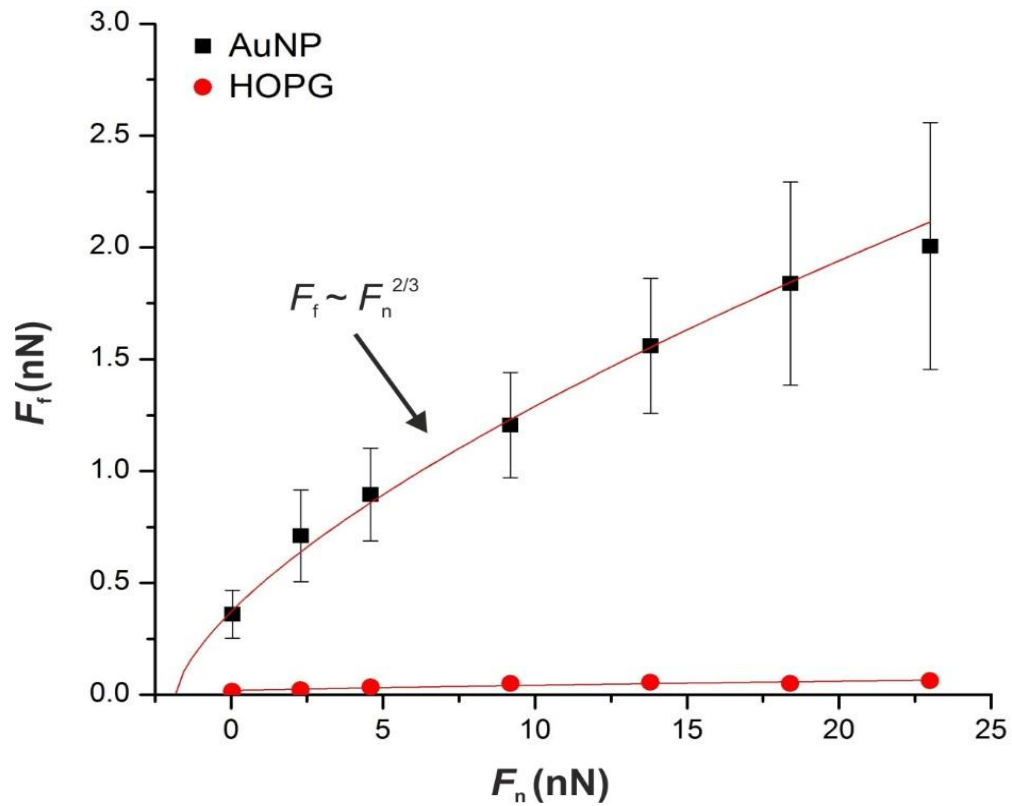


Figure 5.5 Experimental data demonstrating the dependence of friction force (F_f) on normal load (F_n) for AuNPs as well as the HOPG substrate. Image taken from [41].

It should be indicated that the observation of a “2/3” power law pointing towards a Hertzian contact mechanics approach indicates the presence of a tip apex close to a perfect, spherical geometry (i.e., single-asperity) as shown in Figure 5.6 [68].

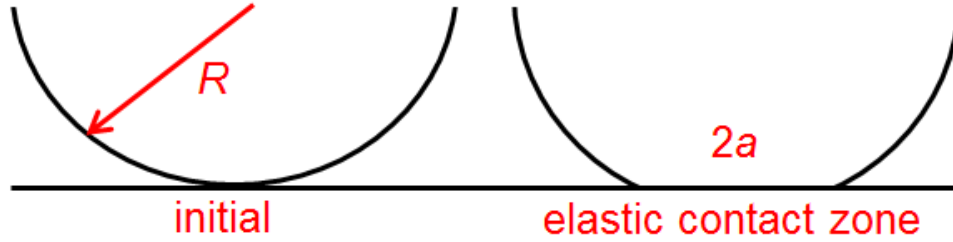


Figure 5.6 An idealized single asperity contact involving a spherical tip apex and a flat surface. The radius of curvature of the asperity is R and the radius of the circular contact area is a .

The contact radius, a , can be specified with the Hertzian contact mechanics approach and it is presumed that it is much smaller than the radius of curvature of the single asperity, R [70]:

$$a^3 = \frac{3 F_N R}{4 E^*} \quad ; \quad a \ll R \quad (5.2)$$

where

$$E^* = \frac{1 - \nu_1^2}{E_1} + \frac{1 - \nu_2^2}{E_2} \quad (5.3)$$

where E_i and ν_i ($i=1,2$) express the Young's moduli and Poisson ratios of the contacting surfaces and F_N is the applied load. Additionally, the friction force can be defined as the ratio of the interfacial shear stress, τ , and the contact area, A [70]:

$$F_f = \tau A \quad (5.4)$$

Finally, by substituting the Equation 5.2 into the Equation 5.4, and assuming that τ is constant, a “2/3” power law dependence of the friction force on the applied load is achieved [70]:

$$F_f = \tau \pi \left(\frac{3}{4} \frac{R}{E^*} \right)^{2/3} F_n^{2/3} \quad (5.5)$$

So, the presented results obtained on AuNPs point towards the existence of a highly spherical and smooth tip apex during the experiments, resulting in the observation of a “2/3” power law dependence of the friction force on the applied load in line with the Hertzian contact mechanics theory.

5.3.2 Dependence of Increased Lateral Forces at AuNP Edges on Normal Load and Particle Height

Topography-caused influences on the friction force during AFM scanning due to sudden changes in the vertical topography of the sample are commonly observed by nanotribology scientists. In order to examine the related effects in quantitative fashion, the AuNP/HOPG material system presents a suitable opportunity due to the readily-available range of AuNP heights between 50-180 nm on the atomically flat, wide terraces of the HOPG substrate. As briefly mentioned before in Section 5.3 and Figure 5.4, the increased lateral forces at AuNP edges ($F_{f,edge}$) are caused by the so-called *ratchet effect* [64]. Additionally, as the AFM tip suddenly encounters the steep slope of a AuNP during scanning, additional twisting is produced by the collision/impact of the tip with the edge (there is a huge amount of height difference between the AuNP and the HOPG substrate at nanoscale) [64].

In conjunction with the comparative analysis of friction forces on the AuNP/HOPG material system, a study of the increased friction forces at the AuNP edges as a function of applied load (F_n) and AuNP height (h) has also been carried out. Experiments performed on 20 separate AuNPs of various heights from 50 nm to 180 nm reveal a gradual increase of $F_{f,edge}$ with particle height (Figure 5.7). Additionally, $F_{f,edge}$ is seen to increase with increasing F_n (Figure 5.8), confirming one of the main predictions of the *ratchet effect* theory [64].

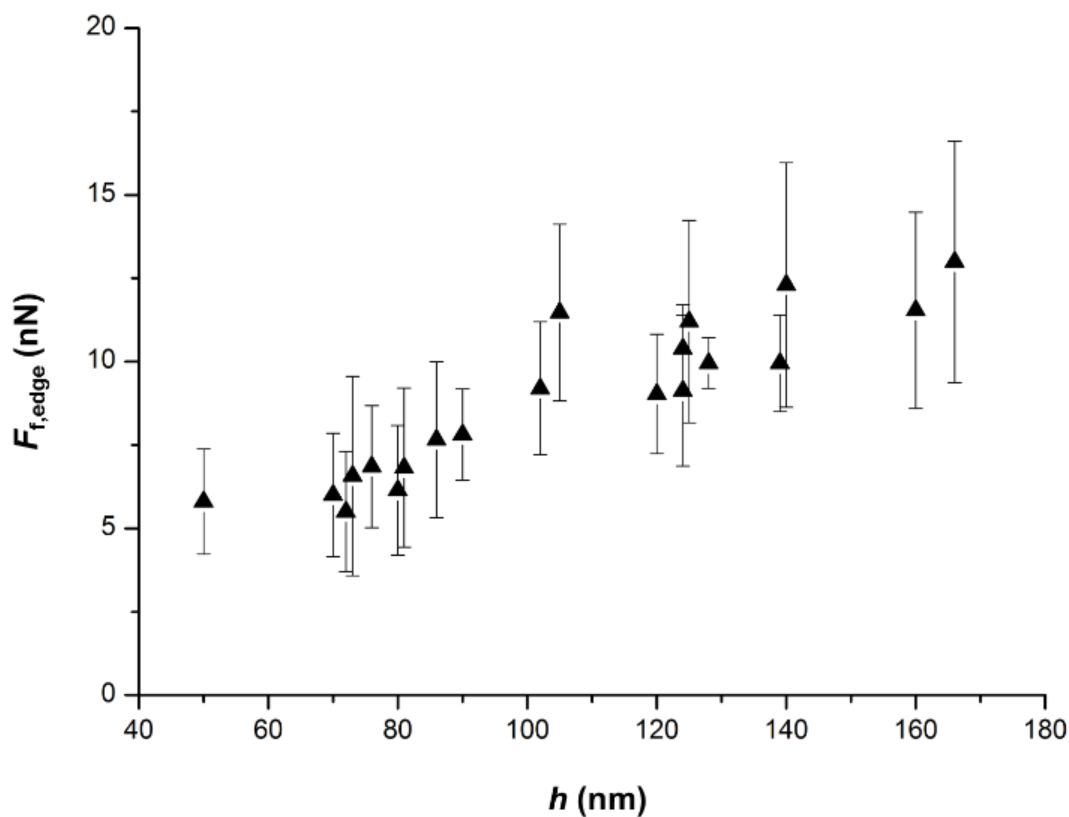


Figure 5.7 Experimental data demonstrating the dependence of increased friction forces at AuNP edges ($F_{f,edge}$) on AuNP height (h), acquired at a fixed normal load of 13.8 nN. The error bars for the friction forces at AuNP edges have been estimated by considering in a multitude of friction force profiles such as the one presented in Figure 5.4(b) along the scanning direction of the cantilever for each individual AuNP at the given constant normal load. Image taken from [41].

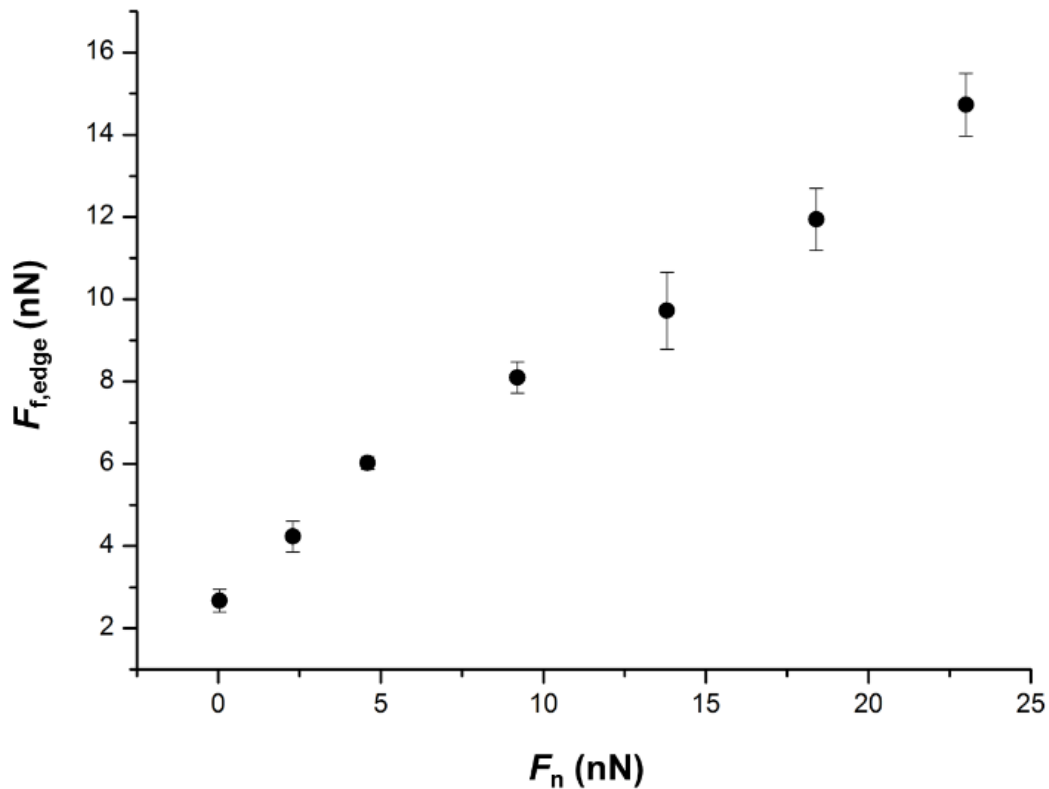


Figure 5.8 Experimental data demonstrating the dependence of increased friction forces at AuNP edges ($F_{f,edge}$) on normal load (F_n) for a representative AuNP with 128 nm height. Image taken from [41].

5.4 Force-Distance Spectroscopy Experiments for the Characterization of Adhesion on AuNPs

As a consequence of the finite adhesion force formed between the tip and cantilever under ambient conditions because of the water meniscus at the tip-sample junction, a non-zero friction force ($0.37 \text{ nN} \pm 0.11 \text{ nN}$) at zero (applied) normal load was encountered in Figure 5.5. As such, the friction force would become zero only at a negative normal load (-1.80 nN). This is equal taken to be equal to the applied *pull-off* force which is essential to overcome the adhesion force

and separate the tip from the sample surface. To quantitatively validate the estimated adhesion force of 1.80 nN, force-distance spectroscopy measurements have been performed on AuNPs on several separate days with the same cantilever (please see Chapter 2 for the details of adhesion measurement via force-distance spectroscopy). Results reveal that the adhesion between the AFM tip and AuNPs is 2.80 ± 1.30 nN, which is in line with our predicted average value of 1.80 nN. Figure 5.9 shows a representative force-distance spectroscopy curve where the adhesion is measured to be ~ 1.6 nN.

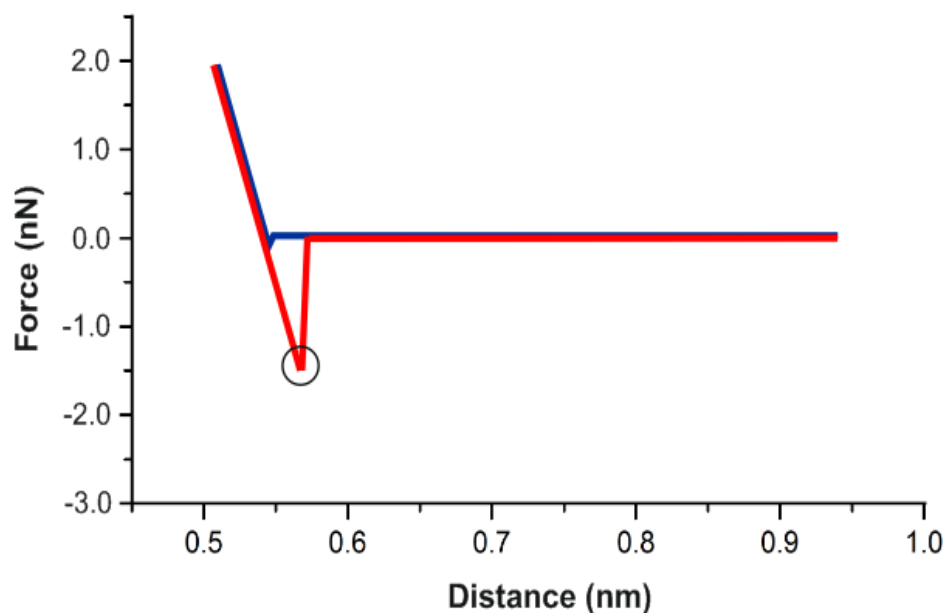


Figure 5.9 A force-distance spectroscopy curve acquired on an individual AuNP. The approach (retract) curve is shown in blue (red). The *pull-off* force (equal in magnitude to adhesion) is highlighted.

Chapter 6

Nano-Manipulation Experiments on the AuNP/HOPG Material System: Contact Area Dependence and Structural Lubricity

6.1 Background

As mentioned in the previous chapter, sliding friction is one of the less understood physical subjects which nevertheless influences our daily lives frequently. Besides, the ability to produce low-friction surfaces can lead to minimize the friction in mobile components in high-technology devices such as NEMS and MEMS. For this purpose, the fundamental mechanisms of friction at the base level (nanoscale) should be investigated via an applicable method. Due to the single asperity nature of the contact formed between the sample surface and the AFM tip, several nanotribology experiments on the effect of normal load, sliding velocity and temperature on friction at the nanoscale have been presented so far [30, 50, 51]. In

addition, phenomena such as *stick slip* [10] and *structural lubricity* [11] have been handled in detail, in some cases together with computational and theoretical studies [71]. The *stick slip* type of motion is encountered as a result of trapped tip apexes at the local potential minima of the measured sample surface whereas the phenomenon of *structural lubricity* is expected to occur when two incommensurate sliding surfaces are in contact where the non-equivalent lattice spacing decreases the potential energy barrier encountered by individual atoms with increasing contact size and leads to very low interfacial friction. Nevertheless, this phenomenon is rarely observed in everyday situations, presumably because of the existence of mobile impurities/dirt molecules under ambient conditions which have a huge impact on interfacial friction [72]. Based on the fact that sliding components featured in both micro/nano- and macro-scale functional devices are typically designed for use under ambient conditions, it is of high importance that the nanotribological characteristics of related material systems are quantified in detail not only under UHV but also under operating conditions (*i.e.* in ambient).

Within the scope of this thesis, lateral nano-manipulation experiments using AFM and nanoparticles (NP) on a flat substrate provide a unique technique to be able to perform frictional characterization of extensive contacts. There are certain nanotribology experiments in the literature based on the intentional lateral manipulation of nanoparticles on structurally well-defined substrates measuring the related frictional forces as a function of contact area [13, 28, 73-75]. The anisotropic friction during sliding of crystalline molybdenum oxide (MoO_3) nanoparticles on the single crystal molybdenum disulfide (MoS_2) surface has been measured [73] while the sliding resistance of both amorphous antimony and crystalline gold nanoparticles on the crystalline HOPG substrate has been investigated by Dietzel and co-workers [28]. Although Ritter *et al.* have obtained a linear relationship between the contact area and the power dissipation needed for translation of antimony particles on HOPG and MoS_2 under ambient conditions

[74], Dietzel *et al.* have found two possible scenarios for the friction behavior of antimony nanoparticles under UHV conditions that they termed *frictional duality*: Some particles exhibit a considerable amount of friction that linearly increases with increasing contact area while some show *superlubric* behavior [75].

Motivated by the background discussion above, nano-manipulation experiments on the AuNP/HOPG material system performed by contact-mode AFM under ambient conditions is presented in this chapter. First, the basic experimental principle is explained and the repeatability of friction forces measured during manipulation is demonstrated for a single AuNP to emphasize the consistency of experimental data. Furthermore, the dependence of friction forces on real contact area for 37 AuNPs is studied where the fact that AuNPs experience ultra-low friction (consistent with the theory of *structural lubricity*) even under ambient conditions is uncovered.

6.2 Manipulation of AuNPs on HOPG

6.2.1 Basic Principle

In order to carry out the experimental studies reported in this chapter, the AuNP/HOPG material system is utilized, the nanotribological characterization of which via contact-mode AFM has been previously described in Chapter 5. The AuNPs are laterally manipulated on the HOPG substrate via contact-mode AFM as illustrated in Figure 6.1. During all lateral manipulation experiments, a single AFM tip which is calibrated with respect to the steps described in Section 5.2 has been used.

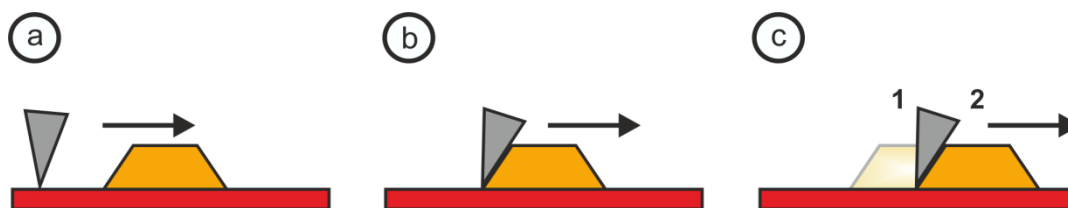


Figure 6.1 Illustration of the AFM tip approaching and manipulating a AuNP on the HOPG substrate. (a) AFM tip scans the HOPG surface and approaches the AuNP, (b) AFM tip reaches the AuNP while the particle is still stationary, (c) manipulation event is achieved and AFM tip pushes the AuNP laterally on the HOPG substrate: (1) before manipulation, (2) after manipulation.

In the literature, the typical parameter leading to the lateral manipulation of a NP is the applied normal force via the AFM tip. Generally, a high normal force results in NP manipulation while a low normal force is not sufficient to manipulate the NP and thus provides only a topographical characterization of the NP as the probe tip moves over it. Therefore, regular topography images of related material systems are typically obtained via contact-mode AFM with low normal forces. If a NP is required to be manipulated, then the cantilever normal force is slightly increased until the NP is pushed laterally.

On the other hand, as already explained in Chapter 5 of this thesis, the AuNPs are very mobile on the HOPG surface and most are readily manipulated during contact-mode scanning, even under very low applied normal forces. As such, this thesis includes the results of lateral manipulation events at *effective zero* applied loads, corresponding to a normal force value that is only related to the adhesion between the AFM tip and the material system. Therefore, lateral manipulation events can be achieved without the application of increased normal forces to the surface. As the AFM tip is pushing a particular AuNP laterally, the corresponding interfacial friction between the AuNP and the HOPG substrate can be inferred from

the increase in the lateral force signal detected via the torsional twisting of the AFM cantilever.

It should be indicated that many *lateral pushing* events that happen spontaneously during contact-mode scanning of the AuNP/HOPG system are hard to analyze quantitatively due to the fact that, (i) the actual size of the AuNP is hard to determine as the particle appears to be *cut* after a manipulation event (see Figure 6.2 (a)) and/or (ii) the line-scan corresponding to the lateral manipulation event cannot be tracked easily, especially in large-scale images with a low density of data points per unit length. As such, focus has been placed on AuNPs that are initially stuck at a single step edge or some other defect, where particle size can be easily determined via initial, small-scale topography scans and subsequent manipulation is achieved after a few passes over the AuNP.

To exemplify the nano-manipulation events, a small-scale topography map recorded at a region of the sample surface containing a single AuNP and the associated topography and lateral force signals before and during manipulation are presented in Figure 6.2. As already mentioned, the particle appears to be *cut* after the manipulation event (described by the orange arrow). While the topography and lateral force signals recorded before the manipulation (along the dashed gray arrow next to the orange one) clearly demonstrate that the tip moves above the AuNP, the flat topography signal during manipulation proves that the tip is pushing the AuNP from the side. The interfacial friction force during the manipulation along the orange arrow in Figure 6.2(a) can be determined from the lateral force signal shown in Figure 6.2(c) where the yellow dashed ellipse indicates the frictional resistance that the AuNP encounters on the HOPG surface (remarkably, <1 nN).

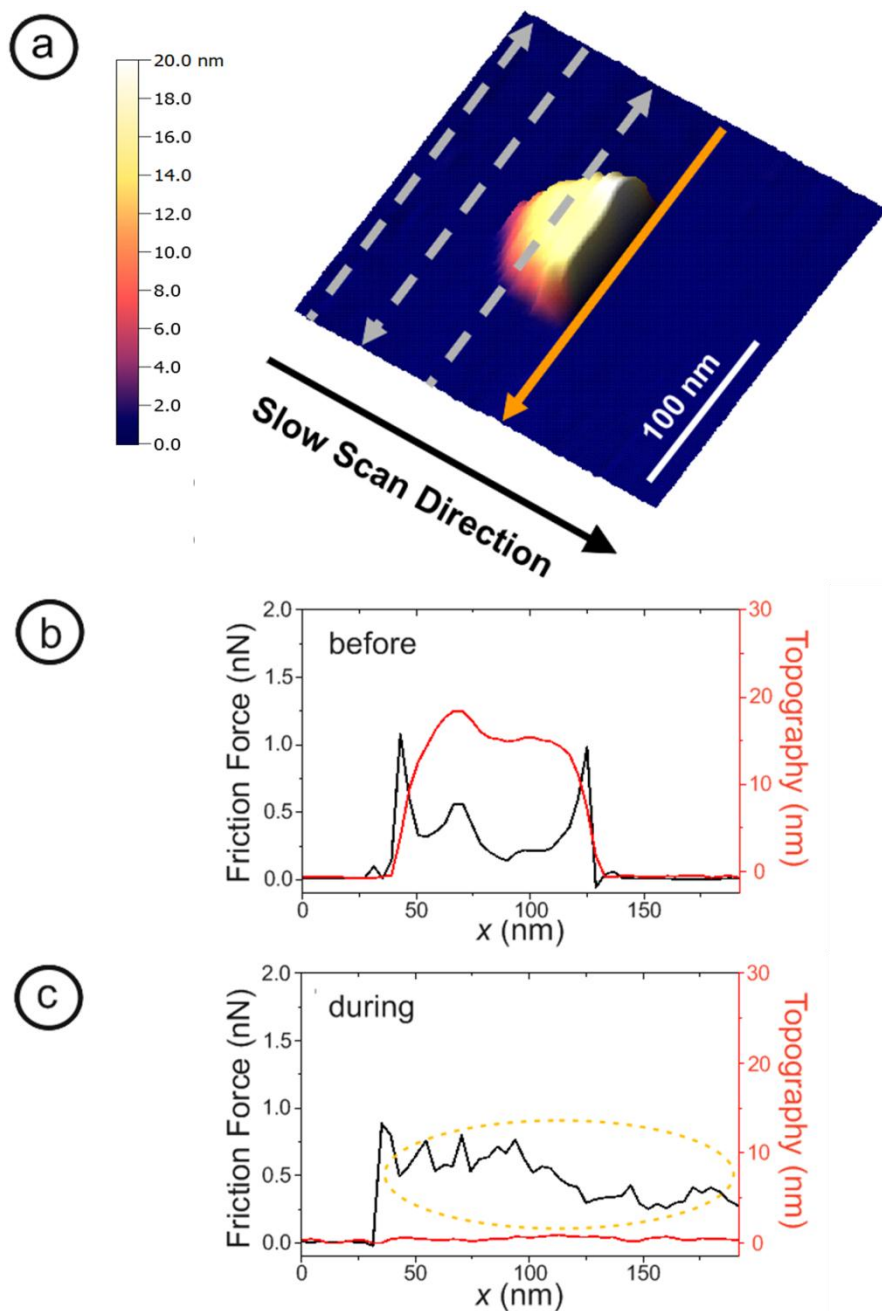


Figure 6.2 (a) Illustration of the lateral manipulation process of a AuNP on the HOPG via contact-mode AFM. Topography and lateral force data measured (b) before and (c) during the manipulation (along the orange arrow) are also given. The yellow dashed ellipse in (c) indicates the frictional resistance that the AuNP encounters on the HOPG surface.

6.2.2 Repeatability

After reviewing the basic principle of the manipulation process, it is necessary to analyze the repeatability of the approach in terms of results. In order to test this aspect, we have focused on an individual AuNP that is repeatedly manipulated between two HOPG steps as illustrated in Figure 6.3.

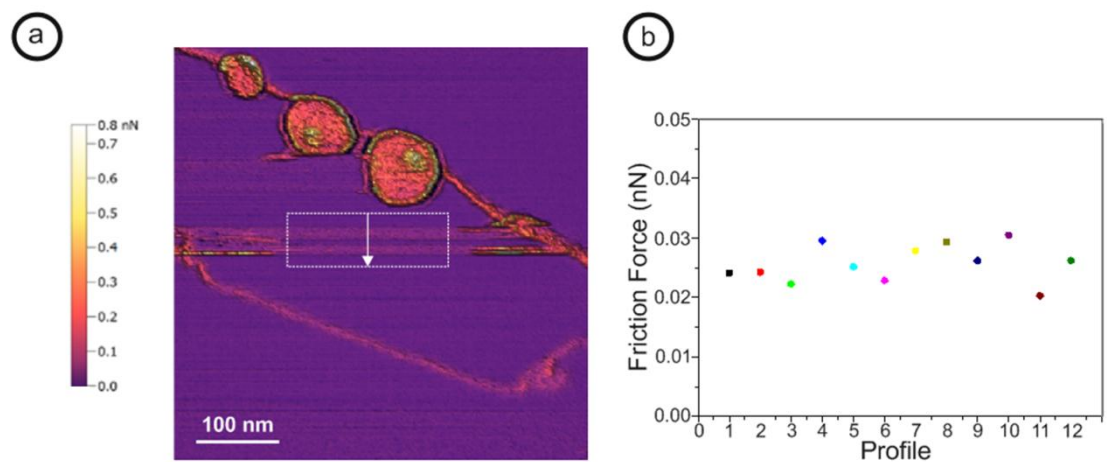


Figure 6.3 Illustration of the repeatable manipulation process of an individual AuNP between two HOPG steps. (a) Lateral force map recorded during the multiple manipulation of the AuNP between two HOPG steps. (b) Average lateral forces extracted for 12 separate profiles taken from the area inside the white dashed rectangle displayed in (a). Please note that the data have been taken from the bright *stripes* in the indicated region, corresponding to increased lateral forces during manipulation.

As shown in Figure 6.3, the same AuNP has been manipulated with *effective zero* applied normal force a total of 12 times between two HOPG steps. The corresponding lateral force map recorded during the manipulation process is presented in Figure 6.3(a) where the frictional contrast between pink manipulation lines and the purple HOPG region can be clearly noticed. Average lateral forces for

12 separate profiles taken from the area inside the white dashed rectangle displayed in Figure 6.3(a) are given in Figure 6.3(b). Consequently, the repeatability of the manipulation process is demonstrated with 12 consistent results of friction force varying between 0.022 and 0.030 nN and an average of 0.0257 nN.

6.3 Contact Area Dependence of Friction: Structural Lubricity under Ambient Conditions

The ratio of lattice constants among two sliding, flat, crystalline surfaces in contact is one of the key parameters that determines interfacial friction since the principle mechanism is based on the fact that individual atoms of the top surface need to overcome the potential energy barriers constituted by the bottom surface atoms for the top surface to be able to laterally move from one location to another. If the two surfaces are *commensurate* (if they have the same lattice constant), then they can periodically *lock* into each other, and under these circumstances, the energy needed to make the surfaces move would increase linearly with increasing number of atoms, as each individual atom of the top surface would have to overcome the same potential energy barrier that a single atom would encounter. On the other hand, if the two surfaces are *incommensurate* and exhibit different lattice constants, then it is not possible for the atoms of the top surface to *fit* into the potential energy wells associated with the bottom surface. As such, the potential energy that each atom needs to overcome for lateral motion decreases with increasing number of atoms, resulting in a dramatic reduction in friction. As previously discussed in Chapter 3, this effect is called *structural lubricity* [30]. As seen from this discussion, the contact area dependence of friction is of vital importance for nanoscale systems.

In order to investigate the contact area dependence of friction, the most applicable method is based on lateral manipulation experiments performed on flat NPs on

atomically flat substrates, where the actual contact area between the NP and the substrate can be accurately determined via contact-mode AFM.

As previously mentioned, friction at the atomic scale depends on the potential energy barrier that the sliding atoms have to surpass to laterally move over the surface. For clean, atomically flat and commensurate surfaces, each sliding atom is exposed to the same amount of potential energy barrier, ΔE , and the total energy barrier, ΔE_{tot} as well as the friction force F is proportional to the number of sliding atoms, N :

$$F = \Delta E_{\text{tot}}/a = (N\Delta E)/a \quad (6.1)$$

where a is the lattice constant along the sliding direction.

On the other hand, if surfaces of the slider and the substrate are incommensurate, lattice constants along the sliding direction become different and each additional sliding atom decreases the potential energy barrier ΔE since the surface potential of the slider *fits* less-well into the surface potential of the substrate with increasing number of sliding atoms [30]. As such, F increases sub-linearly with the number of sliding atoms, N :

$$F = F_0 N^\gamma = \Delta E/a(A\rho)^\gamma \quad (6.2)$$

where the number of sliding atoms, N , is related to contact area A by the equation $N = A\rho$ in which ρ is the number of atoms per unit area at the slider interface [28] and a is now the lattice constant of the substrate. F_0 refers the friction force of a single atom which is found from the diffusion energy barrier, ΔE , divided by the substrate lattice constant, a .

As one can easily observe, Equation 6.2 constitutes a sub-linear *scaling law* for *structurally lubric* sliding of incommensurate interfaces with γ being the scaling power. Analytical calculations and symmetry considerations by Müser *et al.* have

indicated that interfacial friction force for rigid amorphous interfaces is related to the number of sliding atoms such that $\gamma = 0.5$ [72]. Moreover, a scaling law between interfacial friction and contact area for *incommensurate* (nonmatching) crystalline surfaces has also been determined by de Wijn [76]. She has analytically estimated the interfacial friction force between triangular nanocrystals and a hexagonal substrate. With respect to his study, γ can be either 0 or 0.5, depending on the angular orientation of the nanocrystals: $\gamma = 0$ for incommensurate case or $\gamma = 0.5$ for pseudo-commensurate case.

Within the scope of these theoretical considerations, we have analyzed the results of nano-manipulation experiments performed on AuNPs on HOPG under ambient conditions. It is observed that all investigated AuNPs experience remarkably low friction forces during sliding on the HOPG substrate. A detailed study of interfacial friction for 37 AuNPs with respect to contact area is presented in Figure 6.4.

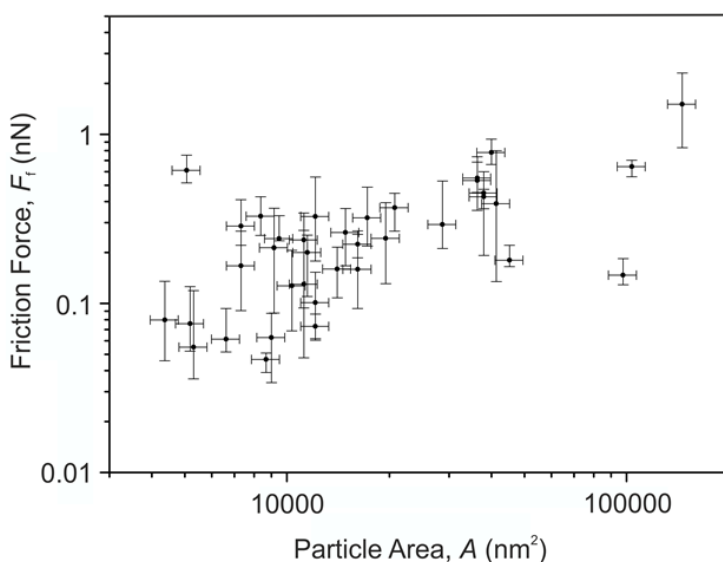


Figure 6.4 Friction forces for 37 AuNPs during sliding on the HOPG substrate as a function of particle contact area. Please note that error bars for the friction force values on AuNPs have been calculated based on fluctuations of lateral force data during manipulation as seen in Figure 6.2 (c).

Subsequent to the detailed analysis of interfacial friction force as a function of contact area for 37 AuNPs, we have normalized the friction force, F , with respect to the single atom friction force F_0 and plotted the normalized friction force (F/F_0) versus the number of interface (sliding) atoms, N , as shown in Figures 6.5 and 6.6.

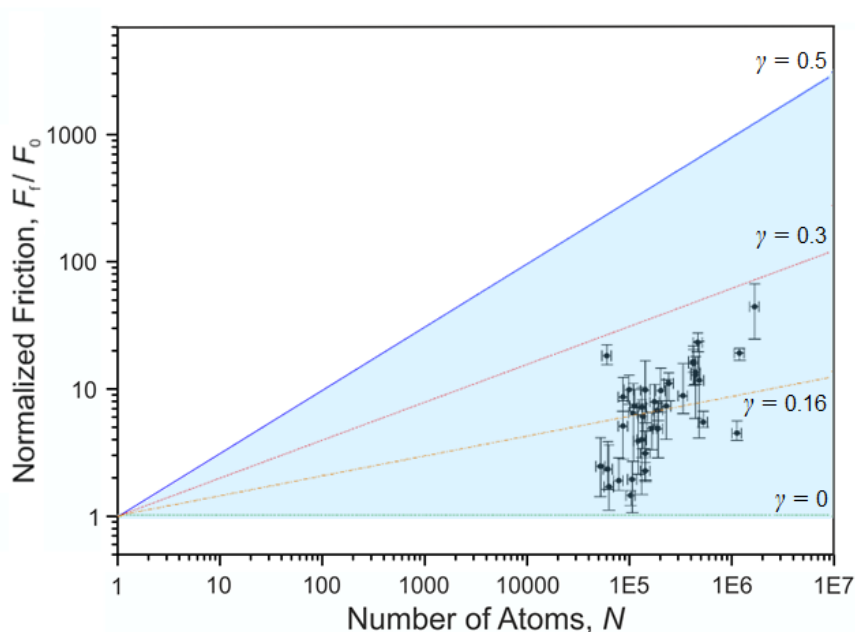


Figure 6.5 Normalized friction data from lateral manipulation experiments plotted as a function of N , the number of atoms on the sliding surface of AuNPs. The friction, F , is normalized by the single atom friction $F_0 = \Delta E/a$ and the number of atoms, N , is estimated from $N = A\rho$. The normalized data points for AuNPs are obtained using $\Delta E = 50$ meV and are in between $\gamma = 0$ and $\gamma = 0.3$, which fits in the *structural lubricity* regime shown by the shaded triangle.

The single atom friction, $F_0 = \Delta E/a$, is calculated from the literature value for the diffusion energy barrier for a single Au atom on HOPG, $\Delta E = 50$ meV [77], and the lattice constant of the HOPG substrate, $a = 2.46$ Å. In order to determine the sliding (interface) atoms per unit area, it is necessary to take into account the crystalline planes at the AuNP/HOPG interface which form during the thermal

growth process. According to our HRTEM results presented in Chapter 4, crystalline AuNPs grow with the (111) plane at the interface and the related atomic density is calculated to $\rho = 14.03$ atoms/nm². As seen in Figure 6.5, the normalized friction data points for all AuNPs lie between $\gamma = 0$ and $\gamma = 0.3$, very clearly fitting the structural lubricity region between $\gamma = 0$ and $\gamma = 0.5$.

In order to check the robustness of the observation of structural lubricity in our experiments with respect to the accuracy of the estimation associated with the theoretical diffusion barrier of $\Delta E = 50$ meV for a single Au atom on HOPG, the experimental data has been plotted with a new, under-estimated diffusion barrier of $\Delta E = 20$ meV (Figure 6.6). As seen in the figure, AuNPs again clearly exhibit the phenomenon of *structural lubricity* even with a very low diffusion barrier of 20 meV, with scaling factors between $\gamma = 0$ and $\gamma = 0.35$.

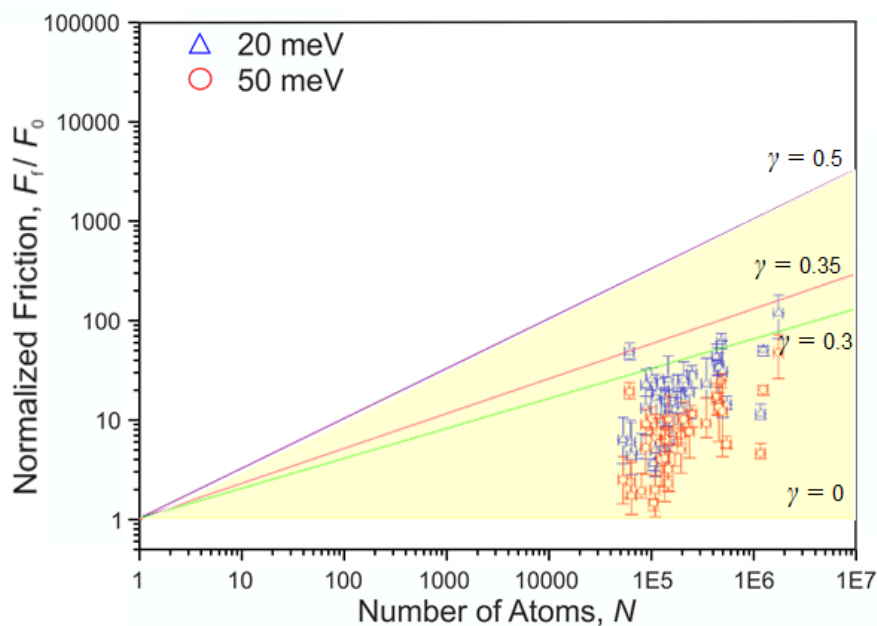


Figure 6.6 Normalized friction data from lateral manipulation experiments plotted as a function of N . The normalized data points for AuNPs are obtained using $\Delta E = 50$ meV (red circle markers) as well as an under-estimated energy barrier of $\Delta E = 20$ meV (blue triangle markers).

In conclusion, our lateral manipulation experiments have confirmed the sub-linear scaling character of friction as a function of contact area for incommensurate interfaces exhibited by the AuNP/HOPG material system, in robust quantitative agreement with the theory of structural lubricity. To illustrate the remarkable tribological character of the material system, it is straightforward to observe that a sliding surface consisting of 1,000,000 Au atoms experiences friction forces that are only expected from <20 Au atoms on HOPG, as seen in Figure 6.5. Our experimental results are remarkable, in the sense that they constitute the first observation of structurally lubric sliding under ambient conditions for a material system that consists of two separate elements. We are projecting that the results presented here will open new avenues for future nanotribology experiments.

Chapter 7

Summary and Outlook

Throughout this thesis, the results of an experimental investigation aimed at a comprehensive *structural and nanotribological characterization* of thermally deposited AuNPs on the HOPG substrate have been presented. Remarkably, nano-manipulation experiments performed on this material system to investigate the *contact area dependence* of friction have led to the observation of the phenomenon of *structural lubricity* under ambient conditions.

In particular:

Well-faceted, hexagonal/elongated-hexagonal AuNPs have been formed upon post-deposition annealing in a quartz furnace at 600-650 °C, in strong contrast to as-deposited thin films exhibiting a channeled, irregular appearance with non-uniform coverage. The crystalline character of the AuNPs has been confirmed via high-resolution TEM imaging and diffraction measurements. To investigate the nanotribological properties of the AuNPs as well as the substrate, AFM measurements performed via a single, calibrated cantilever have been utilized. In contrast to UHV measurements of nanoscale friction on gold surfaces, our measurements performed under ambient conditions point towards a “2/3” power law dependence of friction on normal load for AuNPs, in accordance with the

assumption of a constant shear stress during sliding and Hertzian contact mechanics in the presence of adhesion. Moreover, a study of increased lateral forces at AuNP edges as a function of normal load and particle height has been performed, revealing a linearly proportional dependence for both parameters.

Lateral nano-manipulation experiments using AFM and nanoparticles on a flat substrate provide a unique opportunity to perform a detailed frictional characterization of extensive interfaces. Based on this idea, nano-manipulation experiments on the AuNP/HOPG material system performed by contact-mode AFM under ambient conditions have been reported in this thesis. It has been observed that AuNPs experience remarkably low friction forces during sliding on the HOPG substrate. Within the scope of the relevant theoretical background, a detailed study of friction for 37 AuNPs with respect to the contact area has firmly confirmed the occurrence of *structurally lubric* sliding on the HOPG substrate under ambient conditions.

The results presented in this thesis constitute the first observation of *structurally lubric* sliding under ambient conditions for a material system consisting of two different elements. While very interesting from a fundamental scientific point of view, this observation also holds practical relevance as extensive friction and wear frequently pose significant hurdles to the proper operation of micro/nano-scale machines, and material systems exhibiting structural lubricity under typical operating conditions (*i.e.*, ambient) would prove to be important in this regard. Within this context, we hope that our experiments will pave the way towards a better understanding of friction from a fundamental point of view and also lead to further developments of very low-friction material systems.

Bibliography

- [1] B. Bhushan, “Introduction to Tribology,” *Wiley*, New York, 2013.
- [2] G. Amontons, “De la resistance caus' ee dans les machines,” *Mémoires de l'Académie Royale, A*, Chez Gerard Kuyper, Amsterdam, pp. 257–282, 1706.
- [3] D. Dowson, “History of Tribology,” *Professional Engineering Publishing, 2nd Edition*, London, 1998.
- [4] B. N. J. Persson, “Sliding Friction, Physical Principles and Applications,” *Springer-Verlag Berlin, Heidelberg*, 1998.
- [5] J. A. Greenwood and J. B. P. Williamson, “Contact of Nominally Flat Surfaces,” *Proceedings of the Royal Society of London A*, vol. 295, pp. 300-319, 1966.
- [6] C. M. Mate, G. M. McClelland, R. Erlandsson, and S. Chiang, “Atomic-Scale Friction of a Tungsten Tip on a Graphite Surface,” *Physical Review Letters*, vol. 59, pp. 1942–1945, 1987.
- [7] B. Bhushan, J. N. Israelachvili and U. Landman, “Nanotribology: friction, wear and lubrication at the atomic scale,” *Nature*, vol. 374, pp. 607-616, 1995.
- [8] C. M. Mate, “Tribology on the Small Scale: A Bottom Up Approach to Friction, Lubrication, and Wear,” *Oxford University Press*, Oxford, 2008.
- [9] M. Z. Baykara, T. C. Schwendemann, E. I. Altman and U. D. Schwarz, “Three-Dimensional Atomic Force Microscopy – Taking Surface Imaging to the Next Level,” *Advanced Materials*, vol. 22, pp. 2838–2853, 2010.
- [10] H. Hölscher, U. D. Schwarz, O. Zworner, and R. Wiesendanger, “Consequences of the stick-slip movement for the scanning force microscopy imaging of graphite,” *Physical Review B*, vol. 57, pp. 2477-2482, 1998.
- [11] M. Dienwiebel, G. S. Verhoeven, N. Pradeep, J. W. M. Frenken, J. A. Heimberg and H. W. Zandbergen, “Superlubricity of graphite,” *Physical Review Letters*, vol. 92, pp. 126101- 1-126101-4, 2004.

- [12] D. Dietzel, U. D. Schwarz, A. Schirmeisen, “Nanotribological studies using nanoparticle manipulation: Principles and application to structural lubricity,” *Friction 2*, vol. 2, pp. 114–139, 2014.
- [13] C. Ritter, M. Z. Baykara, B. Stegemann, M. Heyde, K. Rademann, J. Schroers and U. D. Schwarz, “Nonuniform friction-area dependency for antimony oxide surfaces sliding on graphite,” *Physical Review B*, vol. 88, pp. 045422-1-045422-6, 2013.
- [14] G. Binnig, C. F. Quate, and C. Gerber, “Atomic Force Microscope,” *Physical Review Letters*, vol. 56, pp. 930–933, 1986.
- [15] G. Binnig, and H. Rohrer, “Scanning tunneling microscopy,” *Helvetica Physica Acta*, vol. 55, pp. 726–735, 1982.
- [16] P. J. Eaton and P. West, “Atomic Force Microscopy,” *Oxford University Press*, Oxford, 2010.
- [17] <http://www.research.ibm.com/articles/heinrich-rohrer.shtml>
- [18] http://www.nanoscience.ch/nccr/media/sni_newsletter_intern/sninewsIntern_items/2011-12-111212150830/sninewsIntern_long
- [19] http://web.stanford.edu/group/quate_group/
- [20] R. Garcia and R. Perez, “Dynamic atomic force microscopy methods,” *Surface Science Reports*, vol. 47, pp. 197-301, 2002.
- [21] B. Bhushan, “Springer Handbook of Nanotechnology,” Springer-Verlag Berlin, Heidelberg, 2004.
- [22] U. D. Schwarz, P. Koster and R. Wiesendanger, “Quantitative analysis of lateral force microscopy experiments,” *Review of Scientific Instruments*, vol. 67, pp. 2560-2567, 1996.
- [23] M. Endo, T. Hayashi, S. H. Hong, T. Enoki and M. S. Dresselhaus, “Scanning tunneling microscope study of boron-doped highly oriented pyrolytic graphite,” *Journal of Applied Physics*, vol. 90, pp. 5670-5674, 2001.
- [24] M. Ashino, A. Schwarz, H. Hölscher, U. D. Schwarz and R. Wiesendanger, “Interpretation of the atomic scale contrast obtained on graphite and single-

- walled carbon nanotubes in the dynamic mode of atomic force microscopy,” *Nanotechnology*, vol. 16, pp. S134–S137, 2005.
- [25] K. S. Novoselov, D. Jiang, F. Schedin, T. J. Booth, V. V. Khotkevich, S. V. Morozov and A. K. Geim, “Two-dimensional atomic crystals,” *Proceedings of the National Academy of Science USA*, vol. 102, pp. 10451-10453, 2005.
- [26] D. D. L. Chung, “Review Graphite,” *Journal of Materials Science*, vol. 37, pp. 1475–1489, 2002.
- [27] M. Z. Baykara, T. Schwendemann, B. Albers, N. Pilet, H. Mönig, E. Altman, U. D. Schwarz, “Exploring Atomic-Scale Lateral Forces in the Attractive Regime: A Case Study on Graphite (0001),” *Nanotechnology*, vol. 23, pp. 405703-405709, 2012.
- [28] D. Dietzel, M. Feldmann, U. D. Schwarz, H. Fuchs and A. Schirmeisen, “Scaling Laws of Structural Lubricity,” *Physical Review Letters*, vol. 111, pp. 235502-1-235502-5, 2013.
- [29] M. Schirber, “Dragging Nanoparticles Reveals Extra-Low Friction,” *Physics* vol. 6, pp.130, 2013.
- [30] H. Hölscher, A. Schirmeisen and U. D. Schwarz, “Principles of atomic friction: from sticking atoms to superlubric sliding,” *Phil. Trans. R. Soc. A*, vol. 366, pp. 1383-1404, 2008.
- [31] <https://staff.aist.go.jp/nomura-k/common/STRUCIMAGES/Au.gif>
- [32] R. J. Good, L. A. Girifalco, and G. Kraus “A theory for estimation of interfacial energies. II. Application to surface thermodynamics of teflon and graphite,” *Journal of Physical Chemistry*, vol. 62, pp. 1418-1421, 1958.
- [33] H. L. Skriver, and N. M. Rosengaard, “Surface Energy and Work Function of Elemental Metals,” *Physical Review B*, vol. 46, pp. 7157-7168, 1992.
- [34] T. P. Darby and C. M. Wayman, “Nucleation and growth of gold films on graphite: I. Effects of substrate condition and evaporation rate,” *Journal of Crystal Growth*, vol. 28, pp. 41-52, 1975.

- [35] C. M. Wayman and T. P. Darby, "Nucleation and growth of gold films on graphite: II. The effect of substrate temperature," *Journal of Crystal Growth*, vol. 28, pp. 53-67, 1975.
- [36] R. Anton and I. Schneidereit, "In situ TEM investigations of dendritic growth of Au particles on HOPG," *Physical Review B*, vol. 58, pp. 13874- 13881, 1998.
- [37] R. Anton and P. Kreutzer, "In situ TEM evaluation of the growth kinetics of Au particles on highly oriented pyrolytic graphite at elevated temperatures," *Physical Review B*, vol. 61, pp. 16077- 16083, 2000.
- [38] Q. M. Guo, P. Fallon, J. L. Yin, R. E. Palmer, N. Bampos and J. M. Sanders, "Growth of densely packed Au nanoparticles on graphite using molecular templates," *Advanced Materials*, vol. 15, 1084-1087, 2003.
- [39] H. Zhou, F. Yu, M. Chen, C. Qiu, H. Yang, G. Wang, T. Yu and L. Sun, "The transformation of a gold film on few-layer graphene to produce either hexagonal or triangular nanoparticles during annealing," *Carbon*, vol. 52, pp. 379-387, 2013.
- [40] http://unam.bilkent.edu.tr/?al_product=thermal-evaporator
- [41] E. Cihan, A. Özoğul and M. Z. Baykara, "Structure and nanotribology of thermally deposited gold nanoparticles on graphite," *Applied Surface Science*, 2015. DOI: 10.1016/j.apsusc.2015.04.099
- [42] http://unam.bilkent.edu.tr/?al_product=environmental-scanning-electron-microscope-esem
- [43] F. Ruffino and M. G. Grimaldi, "Atomic force microscopy study of the growth mechanisms of nanostructured sputtered Au film on Si(111): Evolution with film thickness and annealing time," *Journal of Applied Physics*, vol. 107, pp. 104321-1-104321-9, 2010.
- [44] <http://www.prothermfurnaces.com/tr/urun-yelpazesi/split-moduler-doner-firinlar/split-firinla>

- [45] Y. F. Mo, K. T. Turner and I. Szlufarska, "Friction laws at the nanoscale," *Nature*, vol. 457, pp. 1116-1119, 2009.
- [46] http://unam.bilkent.edu.tr/tr/?al_product=tem-transmission-electron-microscope
- [47] http://unam.bilkent.edu.tr/tr/?al_product=fib-focused-ion-beam
- [48] J. E. Sader, J. W. M. Chon and P. Mulvaney, "Calibration of rectangular atomic force microscope cantilever," *Review of Scientific Instruments*, vol. 70, pp. 3967-3969, 1999.
- [49] http://unam.bilkent.edu.tr/?al_product=atomic-force-microscope-psia
- [50] R. W. Carpick and M. Salmeron, "Scratching the surface: Fundamental investigations of tribology with atomic force microscopy," *Chemical Reviews*, vol. 97, pp. 1163-1194, 1997.
- [51] I. Szlufarska, M. Chandross and R. W. Carpick, "Recent advances in single-asperity nanotribology," *Journal of Physics D: Applied Physics*, vol. 41, pp.123001-1-123001-39, 2008.
- [52] B. Stegemann, C. Ritter, B. Kaiser, and K. Rademann, "Crystallization of Antimony Nanoparticles: Pattern Formation and Fractal Growth," *Journal of Physical Chemistry B*, vol. 108, pp.14292-14297, 2004.
- [53] N. Vandamme, E. Janssens, F. Vanhoutee, P. Lievens and C. V. Haesendonck, "Scanning probe microscopy investigation of gold clusters deposited on atomically flat substrates," *Journal of Physics: Condensed Matter*, vol. 15, pp. S2983-S2999, 2003.
- [54] N. N. Gosvami, T. Filleter, P. Egberts and R. Bennewitz, "Microscopic friction studies on metal surfaces," *Tribology Letters*, vol. 39, pp. 19-24, 2010.
- [55] R. Bennewitz, F. Hausen and N. N. Gosvami, "Nanotribology of clean and modified gold surfaces," *Journal of Materials Research*, vol. 28, pp. 1279-1288, 2013.

- [56] Q. Y. Li, Y. L. Dong, A. Martini and R. W. Carpick, "Atomic friction modulation on the reconstructed Au (111) surface," *Tribology Letters*, vol. 43, pp. 369-378, 2011.
- [57] J. Sweeney, F. Hausen, R. Hayes, G. B. Webber, F. Endres, M. W. Rutland and R. Bennewitz, "Control of Nanoscale Friction on Gold in an Ionic Liquid by a Potential-Dependent Ionic Lubricant Layer," *Physical Review Letters*, vol. 109, pp. 155502-155506, 2012.
- [58] T. J. Senden and W. A. Ducker, "Experimental determination of spring constants in atomic force microscopy," *Langmuir*, vol. 10, pp. 1003-1004, 1994.
- [59] J. L. Hutter and J. Bechhoefer, "Calibration of atomic-force microscope tips," *Review of Scientific Instruments*, vol. 64, pp. 1868-1873, 1993.
- [60] J. P. Cleveland, S. Manne, D. Bocek, and P. K. Hansma, "A nondestructive method for determining the spring constant of cantilevers for scanning force microscopy," *Review of Scientific Instruments* vol. 64, pp. 403-405, 1993.
- [61] J. E. Sader, I. Larson, P. Mulvaney and L. R. White, "Method for the calibration of atomic force microscope cantilevers," *Review of Scientific Instruments*, vol. 66, pp. 3789-3798, 1995.
- [62] M. Varenberg, I. Etsion and G. Halperin, "An improved wedge calibration method for lateral force in atomic force microscopy," *Review of Scientific Instruments*, vol. 74, pp. 3362-3367, 2003.
- [63] Ogletree, D. F., R. W. Carpick and M. Salmeron, "Calibration of frictional forces in atomic force microscopy," *Review of Scientific Instruments*, vol. 67, pp. 3298-3306, 1996.
- [64] S. Sundararajan, B. Bhushan, "Topography-induced contributions to friction forces measured using an atomic force/friction force microscope," *Journal of Applied Physics*, vol. 88, pp. 4825-4831, 2000.

- [65] U. D. Schwarz, W. Allers, G. Gensterblum and R. Wiesendanger, "Low-load friction behavior of epitaxial C 60 monolayers under Hertzian contact," *Physical Review B*, vol. 52, pp. 14976-14984, 1995.
- [66] U. D. Schwarz, O. Zworner, P. Koster and R. Wiesendanger, "Quantitative analysis of the frictional properties of solid materials at low loads. I. Carbon compounds," *Physical Review B*, vol. 56, pp. 6987-6996, 1997.
- [67] M. Enachescu, R.J. A. van den Oetelaar, R. W. Carpick, D. F. Ogletree and C. F. J. Flipse, "Atomic Force Microscopy Study of an Ideally Hard Contact: The Diamond(111) / Tungsten Carbide Interface," *Physical Review Letters*, vol. 81, pp. 1877-1880, 1998.
- [68] E. Meyer, R. Luthi, L. Howald, M. Bammerlin, M. Guggisberg and H. J. Guntherodt, "Site-specific friction force spectroscopy," *Journal of Vacuum Science & Technology B*, vol. 14, pp. 1285-1288, 1996.
- [69] C.A.J. Putman, M. Igarashi and R. Kaneko, "Single-asperity friction in friction force microscopy: the composite-tip model," *Applied Physics Letters*, vol. 66, pp. 3221-3223, 1995.
- [70] K.L. Johnson, "Contact Mechanics," *Cambridge Univ. Press*, pp. 306-311, 1985.
- [71] N. J. Mosey, M. H. Müser, *Reviews in Computational Chemistry* 25 (2007) 67.
- [72] M. H. Müser, L. Wenning, and M. O. Robbins, "Simple Microscopic Theory of Amontons' Laws for Static Friction," *Physical Review Letters*, vol. 86, pp. 1295-1298, 2001.
- [73] P.E. Sheehan and C.M. Lieber, "Nanotribology and nanofabrication of MoO₃ structures by force microscopy," *Science*, vol. 272, pp. 1158-1161, 1996.
- [74] C. Ritter, M. Heyde, B. Stegemann, K. Rademann, U. D. Schwarz, "Contact-area dependence of frictional forces: Moving adsorbed antimony nanoparticles," *Physical Review B*, vol. 71, pp. 085405-1-085405-7, 2005.

- [75] D. Dietzel, C. Ritter, T. Monninghoff, H. Fuchs, A. Schirmeisen, U. D. Schwarz, “Frictional Duality Observed during Nanoparticle Sliding,” *Physical Review Letters*, vol. 101, pp.125505-125508, 2008.
- [76] A. S. de Wijn, “(In)commensurability, scaling, and multiplicity of friction in nanocrystals and application to gold nanocrystals on graphite,” *Physical Review B*, vol. 86, pp. 085429-1-085429-11, 2012.
- [77] M. Hirano, K. Shinjo, R. Kaneko, and Y. Murata, “Observation of superlubricity by scanning tunneling microscopy,” *Physical Review Letters*, vol. 78, pp. 1448-1451, 1997.